

**DIRECT COMPARISONS OF POLARIMETRIC C-BAND AND
S-BAND MOMENTS IN SNOW**

BRANDON M. TAYLOR

A THESIS SUBMITTED TO THE FACULTY OF GRADUATE STUDIES
IN PARTIAL FULFILMENT OF THE REQUIREMENTS
FOR THE DEGREE OF

MASTER OF SCIENCE

GRADUATE PROGRAM IN EARTH AND SPACE SCIENCE
YORK UNIVERSITY
TORONTO, ONTARIO
APRIL 2018

**DIRECT COMPARISONS OF
POLARIMETRIC C-BAND AND S-BAND
MOMENTS IN SNOW**

by **Brandon M. Taylor**

a thesis submitted to the Faculty of Graduate Studies of
York University in partial fulfilment of the requirements
for the degree of

MASTER OF SCIENCE
© 2018

Permission has been granted to: a) YORK UNIVERSITY LIBRARIES to lend or sell copies of this dissertation in paper, microform or electronic formats, and b) LIBRARY AND ARCHIVES CANADA to reproduce, lend, distribute, or sell copies of this thesis anywhere in the world in microform, paper or electronic formats *and* to authorise or procure the reproduction, loan, distribution or sale of copies of this thesis anywhere in the world in microform, paper or electronic formats.

The author reserves other publication rights, and neither the thesis nor extensive extracts for it may be printed or otherwise reproduced without the author's written permission.

DIRECT COMPARISONS OF POLARIMETRIC C-BAND AND S-BAND MOMENTS IN SNOW

by **Brandon M. Taylor**

By virtue of submitting this document electronically, the author certifies that this is a true electronic equivalent of the copy of the thesis approved by York University for the award of the degree. No alteration of the content has occurred and if there are any minor variations in formatting, they are as a result of the conversion to Adobe Acrobat format (or similar software application).

Examination Committee Members:

1. George Isaac
2. Dave Sills
3. Peter Taylor
4. Fourth Examiner
5. Fifth Examiner
6. Sixth Examiner

Abstract

Calibrating weather radars is an ongoing issue, and as radar networks age and requirements change, new methods will continue to be developed to address these issues. When the United States WSR-88D NEXRAD weather radar network was upgraded to dual-polarimetric capabilities from 2011-2013, there was a flurry of effort to handle the calibration requirements of the new equipment. Techniques for the estimating bias of differential reflectivity (Z_{DR}) using external targets were developed to verify that the internal calibration procedures performed as expected. With the calibration of one radar known, it can be compared with another to verify the others performance. In this case, the National Weather Service Buffalo, NY WSR-88D is compared with its neighbor to the north, Environment Canada's King City radar. Comparisons are performed during two different subsets of precipitation events, those being synoptic and lake-effect snow events. The data are analyzed onto a common grid using a distance-weighting scheme, with a hydrometeor classification scheme used to filter for dry snow. It is shown that the agreement between the radars in terms of reflectivity is within the bounds of the canonical 1 dB bias threshold. Furthermore, while the previous external target method relies on the self-consistency principle and is only able to detect a negative bias, this method brings in an independent set of observations to diagnose both positive and negative biases.

Table of Contents

Abstract	iv
Table of Contents	v
List of Figures	vii
1 Chapter One	1
1.1 Introduction	1
1.2 Background	2
1.2.1 Reflectivity Factor (Z_h)	2
1.2.2 Differential Reflectivity (Z_{dr})	3
2 Chapter Two	5
2.1 Methodology	5
2.1.1 Comparison of Radar Systems	5
2.1.2 Distance-Weighting Scheme	7
2.2 Selection of Cases	9
2.3 Filtering Conditions	10
2.3.1 Time Filter	10
2.3.2 Gate Filters	11
2.4 Advanced Statistical Techniques	11

2.4.1	Kernel Density Estimation	11
2.4.2	Orthonormal Linear Regression	12
2.5	Z_{DR} Bias Estimation	13
3	Chapter Three	15
3.1	Event Comparisons	15
3.1.1	18 January 2014 - Synoptic	15
3.1.2	23 January 2014 - Lake-Effect	18
3.1.3	1 February 2014 - Synoptic	21
3.1.4	6 January 2015 - Lake-Effect	24
3.1.5	7 January 2015 - Synoptic	26
3.1.6	6 February 2015 - Synoptic	29
3.1.7	14 February 2015 - Lake-Effect	31
3.1.8	18 February 2015 - Lake-Effect	34
3.1.9	10 February 2016 - Lake-Effect	36
3.1.10	15 December 2016 - Synoptic	39
3.2	Z_{eH} Subset Comparisons	42
A	Appendix A	44
A.1	Upper-Air Charts	44
A.2	Skew-T Charts	44
A.3	Sounding Climatology	44
Bibliography		66

List of Figures

1.1	The location of the NWS Buffalo Radar (KBUF) and King City Radar (CWKR) are shown as red dots, with a 75 km range ring around each.	4
2.1	Bounding box of the study area, denoted by the green shading. (latitude, longitude) given for each corners.	6
2.2	Base moment comparisons between radars over Lake Ontario, with dimensions of 20x12.5 km. Left panels are in native radars coordinates, with gates outlined in black. Right panels are transformed to a common Cartesian grid, with grid cells outlined in black.	8
2.3	Illustration of the construction of 2D kernel density estimates. (Left) data points with individual kernels as grey dashed lines, (right) summed kernels = kernel density estimate.	12
2.4	Demonstration of an Orthonormal Linear Regression	13
3.1	Gridded Z_{eH} comparison for 18 January 2014. Time-average of all admitted scans.	16
3.2	Gridded Z_{DR} comparison for 18 January 2014. Time-average of all admitted scans.	16

3.3	Direct comparisons for 18 January 2014. Dataset includes all admitted grid cells.	17
3.4	Histograms of Z_{DR} (left), Z_{DR} bias at CWKR, determined by subtracting the gridded, bias adjusted Z_{DR} at KBUF from the Z_{DR} at CWKR. Both datasets exclude matched points with KDE < 2.	18
3.5	Gridded Z_{eH} comparison for 23 January 2014. Time-average of all admitted scans.	19
3.6	Gridded Z_{DR} comparison for 23 January 2014. Time-average of all admitted scans.	19
3.7	Direct comparisons for 23 January 2014. Dataset includes all admitted grid cells.	20
3.8	Histograms of Z_{DR} (left), Z_{DR} bias at CWKR, determined by subtracting the gridded, bias adjusted Z_{DR} at KBUF from the Z_{DR} at CWKR. Both datasets exclude matched points with KDE < 2.	21
3.9	Gridded Z_{eH} comparison for 1 February 2014. Time-average of all admitted scans.	22
3.10	Gridded Z_{DR} comparison for 1 February 2014. Time-average of all admitted scans.	22
3.11	Direct comparisons for 1 February 2014. Dataset includes all admitted grid cells.	23
3.12	Histograms of Z_{DR} (left), Z_{DR} bias at CWKR, determined by subtracting the gridded, bias adjusted Z_{DR} at KBUF from the Z_{DR} at CWKR. Both datasets exclude matched points with KDE < 2.	23
3.13	Gridded Z_{eH} comparison for 6 January 2015. Time-average of all admitted scans.	24

3.14 Gridded Z_{DR} comparison for 6 January 2015. Time-average of all admitted scans.	25
3.15 Direct comparisons for 6 January 2015. Dataset includes all admitted grid cells.	25
3.16 Histograms of Z_{DR} (left), Z_{DR} bias at CWKR, determined by subtracting the gridded, bias adjusted Z_{DR} at KBUF from the Z_{DR} at CWKR. Both datasets exclude matched points with KDE < 2.	26
3.17 Gridded Z_{eH} comparison for 7 January 2015. Time-average of all admitted scans.	27
3.18 Gridded Z_{DR} comparison for 7 January 2015. Time-average of all admitted scans.	27
3.19 Direct comparisons for 7 January 2015. Dataset includes all admitted grid cells.	28
3.20 Histograms of Z_{DR} (left), Z_{DR} bias at CWKR, determined by subtracting the gridded, bias adjusted Z_{DR} at KBUF from the Z_{DR} at CWKR. Both datasets exclude matched points with KDE < 2.	28
3.21 Gridded Z_{eH} comparison for 6 February 2015. Time-average of all admitted scans.	29
3.22 Gridded Z_{DR} comparison for 6 February 2015. Time-average of all admitted scans.	30
3.23 Direct comparisons for 6 February 2015. Dataset includes all admitted grid cells.	30
3.24 Histograms of Z_{DR} (left), Z_{DR} bias at CWKR, determined by subtracting the gridded, bias adjusted Z_{DR} at KBUF from the Z_{DR} at CWKR. Both datasets exclude matched points with KDE < 2.	31

3.25 Gridded Z_{eH} comparison for 14 February 2015. Time-average of all admitted scans.	32
3.26 Gridded Z_{DR} comparison for 14 February 2015. Time-average of all admitted scans.	32
3.27 Direct comparisons for 14 February 2015. Dataset includes all admitted grid cells.	33
3.28 Histograms of Z_{DR} (left), Z_{DR} bias at CWKR, determined by subtracting the gridded, bias adjusted Z_{DR} at KBUF from the Z_{DR} at CWKR. Both datasets exclude matched points with KDE < 2.	33
3.29 Gridded Z_{eH} comparison for 18 February 2015. Time-average of all admitted scans.	34
3.30 Gridded Z_{DR} comparison for 18 February 2015. Time-average of all admitted scans.	35
3.31 Direct comparisons for 18 February 2015. Dataset includes all admitted grid cells.	35
3.32 Histograms of Z_{DR} (left), Z_{DR} bias at CWKR, determined by subtracting the gridded, bias adjusted Z_{DR} at KBUF from the Z_{DR} at CWKR. Both datasets exclude matched points with KDE < 2.	36
3.33 Gridded Z_{eH} comparison for 10 February 2016. Time-average of all admitted scans.	37
3.34 Gridded Z_{DR} comparison for 10 February 2016. Time-average of all admitted scans.	37
3.35 Direct comparisons for 10 February 2016. Dataset includes all admitted grid cells.	38

3.36	Histograms of Z_{DR} (left), Z_{DR} bias at CWKR, determined by subtracting the gridded, bias adjusted Z_{DR} at KBUF from the Z_{DR} at CWKR. Both datasets exclude matched points with KDE < 2.	39
3.37	Gridded Z_{eH} comparison for 15 December 2016. Time-average of all admitted scans.	40
3.38	Gridded Z_{DR} comparison for 15 December 2016. Time-average of all admitted scans.	40
3.39	Direct comparisons for 15 December 2016. Dataset includes all admitted grid cells.	41
3.40	Histograms of Z_{DR} (left), Z_{DR} bias at CWKR, determined by subtracting the gridded, bias adjusted Z_{DR} at KBUF from the Z_{DR} at CWKR. Both datasets exclude matched points with KDE < 2.	41
3.41	Scatter-plots of CWKR versus KBUF grid analyzed reflectivity, with Kernel Density Estimation shading. The red line is an Orthonormal Linear Regression, with a black identity line.	43
A.1	500mb Geopotential Height at 06Z 18 January 2014.	45
A.2	500mb Geopotential Height at 06Z 23 January 2014	46
A.3	500mb Geopotential Height at 18Z 1 February 2014.	47
A.4	500mb Geopotential Height at 15Z 6 January 2015.	48
A.5	500mb Geopotential Height at 09Z 7 January 2015.	49
A.6	500mb Geopotential Height at 09Z 6 February 2015.	50
A.7	500mb Geopotential Height at 12Z 14 February 2015.	51
A.8	500mb Geopotential Height at 21Z 18 February 2015.	52
A.9	500mb Geopotential Height at 18Z 10 February 2016.	53
A.10	500mb Geopotential Height at 09Z 15 December 2016.	54

A.11 SkewT/Log-P Chart from the BUF Radiosonde launched at 12Z 18 January 2014	55
A.12 SkewT/Log-P Chart from the BUF Radiosonde launched at 00Z 23 January 2014	56
A.13 SkewT/Log-P Chart from the BUF Radiosonde launched at 12Z 1 February 2014	57
A.14 SkewT/Log-P Chart from the BUF Radiosonde launched at 00Z 6 January 2015	58
A.15 SkewT/Log-P Chart from the BUF Radiosonde launched at 12Z 7 January 2015	59
A.16 SkewT/Log-P Chart from the BUF Radiosonde launched at 00Z 6 February 2015	60
A.17 SkewT/Log-P Chart from the BUF Radiosonde launched at 12Z 14 February 2015	61
A.18 SkewT/Log-P Chart from the BUF Radiosonde launched at 00Z 18 February 2015	62
A.19 SkewT/Log-P Chart from the BUF Radiosonde launched at 12Z 10 February 2016	63
A.20 SkewT/Log-P Chart from the BUF Radiosonde launched at 12Z 15 December 2016	64
A.21 Sounding Precipitable Water Climatology for BUF	65

1 Chapter One

1.1 Introduction

Weather radar is an invaluable tool for hydrometeorological purposes; with the refinement of operational polarimetric radars, it has become indispensable for quantitative precipitation estimation (QPE). Numerous studies have shown the skill of dual-pol estimators over traditional reflectivity-based algorithms, especially for rainfall cases. One approach is using polarimetric moments directly in empirically derived power law relations. Previously, two relations were developed by Hassan et al. (2017) ; one using just horizontal reflectivity (Z_H), while the other incorporated differential reflectivity (Z_{DR}) from the polarimetric C-Band radar at King City (CWKR). These algorithms were correlated with ground measurements of snowfall accumulation. The conclusion from the previous dataset is that the addition of Z_{DR} did not significantly improve the SWE estimates, but both still performed better than the legacy algorithm used by Environment Canada. Another approach for improving QPE estimates through polarimetric data is the classification of hydrometeor types, then using a corresponding relation matched to that type. While quantitative precipitation estimates contain statistical measurement error propagated from Z and Z_{DR} , this error is reduceable through spatial and temporal smoothing. Meanwhile, smoothing will not remove biases in the moments. This error will be propagated into QPE estimates, which is why its important to

remove them. Here, it is shown that with biased Z_{DR} is used as input into Colorado State University hydrometeor classification scheme, it is successful at filtering for similar dry snow targets in synoptic snowfall events with temperatures within the plate growth region, while failing in lake-effect snow events. The purpose of the filtering is to yield better estimates of systematic bias.

1.2 Background

First, it is important to provide some background on the weather radar moments that are presented in this study, from both single and dual polarized signals. The convention for representing these moments symbolically hereafter is lower-case subscript for linear units and upper-case subscript for logarithmic units, i.e. Z_{DR} is logarithmic while Z_{dr} is linear.

1.2.1 Reflectivity Factor (Z_h)

$$Z_h = \int_0^\infty N(D)D^6 dD \text{ (mm}^6/\text{m}^3\text{)} \quad (1.1)$$

The foremost moment derived from radar is the reflectivity factor (Z_h), where the subscript denotes its derivation from the horizontally polarized signal. This variable measures the number density $N(D)$ of hydrometeors of diameter D per unit volume, as presented in Equation 1.1. Due to uncertainties about what type of target is actually doing the scattering, it is typically represented as the equivalent reflectivity factor Z_{eh} , where $Z_h = Z_{eh}$ if the targets are made of liquid water and are comparatively small to the wavelength (Fabry 2015). The two names are essentially interchangeable, but the nomenclature Z_{eh} will be used in this study to acknowledge the presence of non-ideal targets, e.g. snow crystals.

1.2.2 Differential Reflectivity (Z_{dr})

Radars equipped with dual-polarimetric (dual-pol) capabilities are still an emerging technology, in terms of operational meteorological applications. These types of radar systems are capable of transmitting and receiving two orthogonally polarized electromagnetic waves in order to deduce more information about the microphysical structure of hydrometeors. One of the main variables this allows them to produce is Z_{DR} , defined as the ratio of the horizontal channel reflectivity (Z_H) to the vertical channel reflectivity (Z_V). This can be simplified to the difference between the two using the logarithmic quotient rule, since they are represented in logarithmic units. Equation 1.2 demonstrates this concept.

$$Z_{dr} = 10 * \log_{10}\left(\frac{Z_H}{Z_V}\right) = Z_h - Z_v \quad (1.2)$$

Although dual-pol radar has matured within the research community, operational deployment has been a much slower process. Many studies have been undertaken in regards to quantitative precipitation estimation using dual-pol variables for rainfall, but studies involving the estimation of snowfall liquid equivalent has been much more limited. In Canada, there is one active C-band weather radar with dual-pol capabilities. It is located north of Toronto, in King City, with rest of the network is currently undergoing an upgrade to polarimetric S-Band. Its neighbor to the south, KBUF, was upgraded to dual-pol in 2012 as part of a network wide upgrade. Figure 1.1 shows the geographic location of the radar sites in comparison with each other.

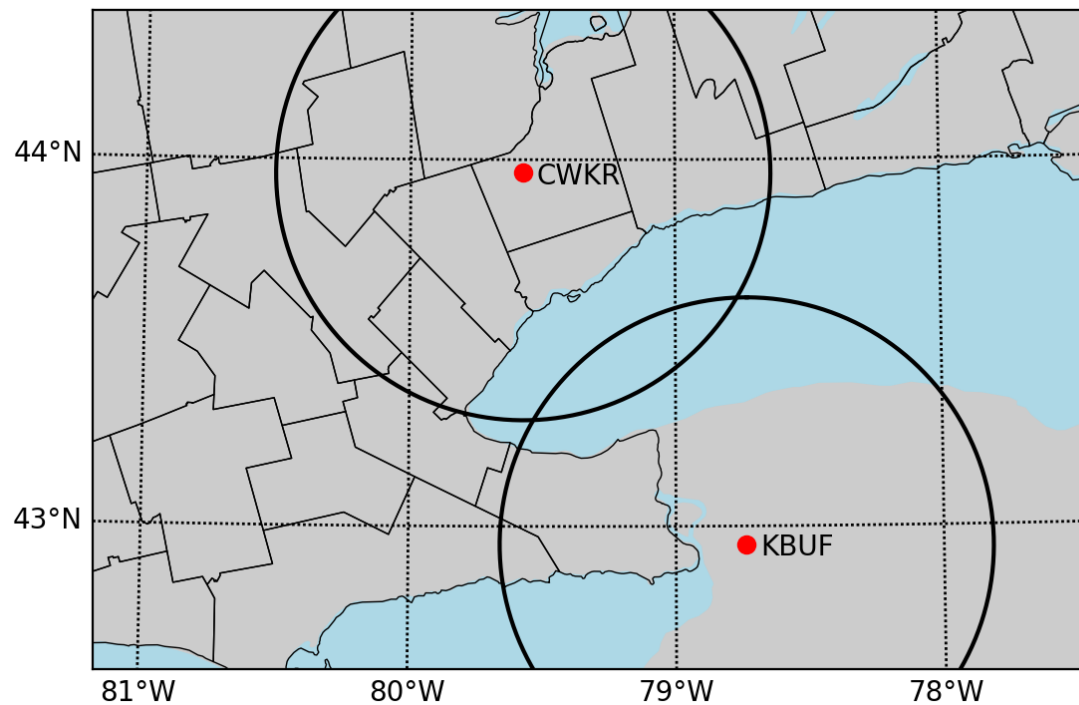


Figure 1.1: The location of the NWS Buffalo Radar (KBUF) and King City Radar (CWKR) are shown as red dots, with a 75 km range ring around each.

2 Chapter Two

2.1 Methodology

2.1.1 Comparison of Radar Systems

Comparing two radar datasets is fraught with challenges; solutions to meet this challenge are presented herein. Even though the radar system characteristics are not identical, the measurements are comparable due to the design of the weather radar equation, which accounts for the sensitivity of the radar system itself (Rogers and Yau 1989). The area of study was chosen to ensure that the coinciding radar scans had similar resolution samples and beam heights. Lake Ontario happens to be the perfect area to bound between the radars, therefore only data from areas over water inside the bounding box depicted in Figure 2.1 are used. This also ensures that no ground clutter is incorporated into the analyses.

2.1.1.1 Comparing Radar Characteristics

$$\bar{P}_r = \frac{\pi^3 c}{1024 \ln(2)} \left[\frac{P_t \tau G^2 \theta^2}{\lambda^2} \right]_{dBZ_0} \left[|K^2| \frac{Z_{eH}}{r^2} \right]_{TARGET} \quad (2.1)$$

As presented in Equation 2.1, the weather radar equation is defined by constant parameters dependent on the radar system characteristics, and varying properties related to the target. The target properties are dielectric constant (K), range (r) and equivalent reflectivity factor Z_{eH} . Conversely, the radar parameters ideally

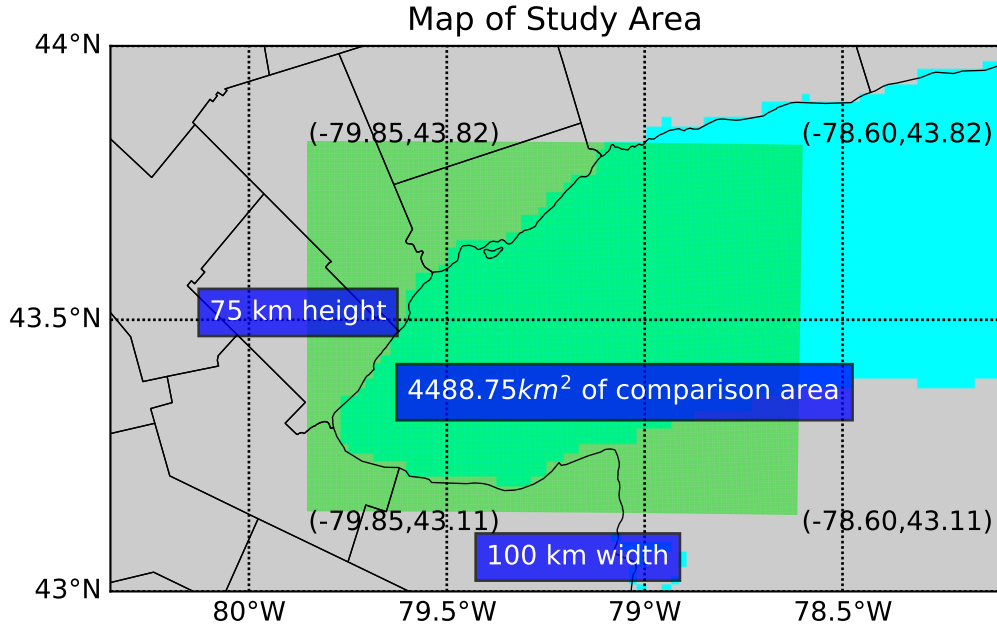


Figure 2.1: Bounding box of the study area, denoted by the green shading. (latitude, longitude) given for each corners.

remain unchanged from their values upon installation of the radar system. These parameters form the radar constant, symbolically expressed as dBZ_0 . The parameters that define this constant include the power transmitted (P_t), the pulse length (τ), the antenna gain (G), the angular beamwidth (θ), and the wavelength (λ).

$$10 \log Z = 10 \log \bar{P}_r + 20 \log r - dBZ_0 \quad (2.2)$$

Equation 2.2 shows how dBZ_0 is subtracted out from the full calculation of Z . Table 2.1 compares these parameters for both radar systems. The biggest difference between the two is the wavelength, with CWKR operating in the C frequency band and KBUF operating in the S frequency band. It should be noted that although KBUF has a larger physical beamwidth than CWKR, it achieves an effective azimuthal resolution of 0.5° through an over-sampled data windowing technique (Torres and Curtis 2007). Therefore, the two radars are matched in

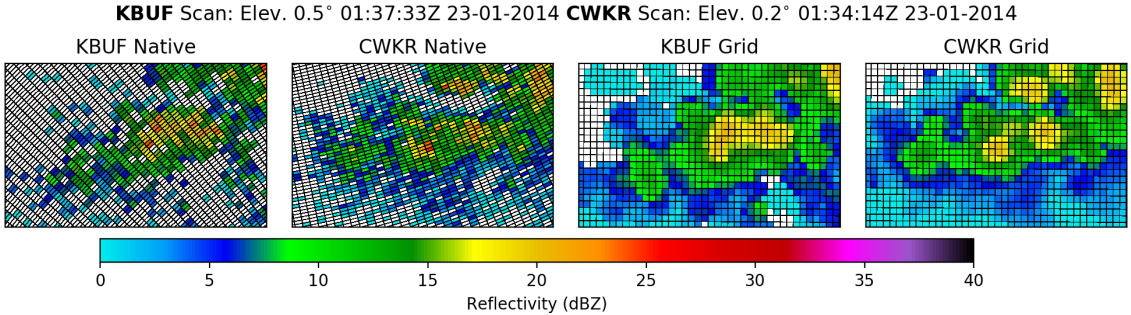
azimuthal resolution, while CWKR has twice the range resolution of KBUF. Also, it should be stated that the signal processors used in both radar systems are in the Vaisala SIGMET series, therefore they measure Z_{eH} and Z_{DR} using 8 bit resolution. With data intervals of -31.5 dBZ to +95.5 dBZ and -7.94 dB to +7.94 dB, This equates to a data resolution of 0.5 dBZ and 0.0625 dB, respectively.

Table 2.1: Specifications of each radars system, with symbols as used in Eq. 2.2

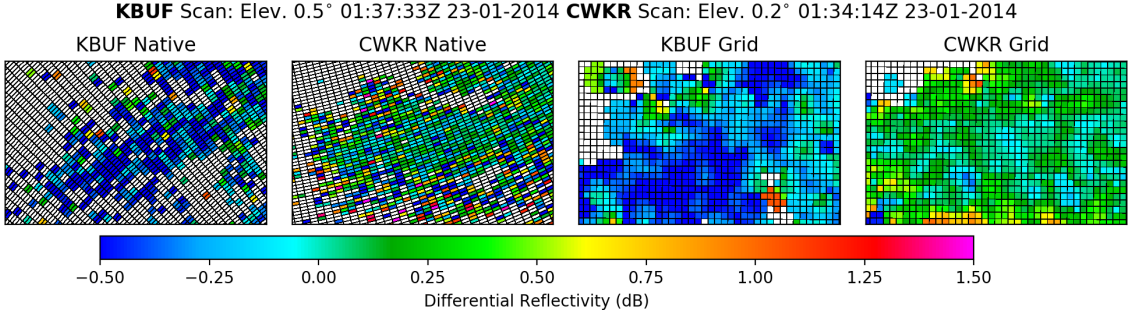
field [symbol](unit)	King City (CWKR)	Buffalo (KBUF)
Wavelength [λ](cm)	5 (C-Band)	10 (S-Band)
Beamwidth [θ] ($^{\circ}$)	0.62	0.92
Antenna Gain [G] (dB)	45.5	49.2
Transmitter Peak Power (kW)	250	1000
Pulse Length [τ] (μs)	0.8/2.0	1.5/4.5
Matched Elevation Angle ($^{\circ}$)	0.2	0.5
Range Resolution [r] (m)	125	250

2.1.2 Distance-Weighting Scheme

The biggest challenge when comparing radar resolution volumes measured by radars that are not co-located is resolving the differences in coordinate system. A resolution volume is defined as volume irradiated by the idealized Gaussian beam pattern for each range gate, otherwise known as a bin. Resolution volumes are sampled natively in the spherical coordinate system; although there may be some overlap, the shape of the bins will vary drastically. Differences between KBUF and CWKR bin geometry can be ascertained from Figure 2.2.



(a) Z_H comparison, shows the smooth transformation from an isotropic input to an isotropic gridded output.



(b) Z_{DR} comparison, in contrast with (a), shows the limitations of representing an anisotropic field with an isotropic distance-weighting function.

Figure 2.2: Base moment comparisons between radars over Lake Ontario, with dimensions of 20x12.5 km. Left panels are in native radars coordinates, with gates outlined in black. Right panels are transformed to a common Cartesian grid, with grid cells outlined in black.

These differences require the radar data to be objectively analyzed onto a common coordinate system, which can be achieved through a distance-weighting scheme. , which essentially convolves radar data with a distance-weighted function. This method was adopted in a more recent open source software module called the Python ARM Radar Toolkit (Py-ART) (Helmus and Collis 2016), which is used here. In accordance with the recommendations of Pauley and Wu (1990), a grid

resolution (Δx , Δy) of 500 meters is chosen. A Barnes distance-weighting scheme is used for this analysis.

$$F_{i,j} = \sum_0^n F(b) * e^{-(d/ROI)^2} \quad (2.3)$$

The Gaussian weighting function used in said scheme is given in Equation 2.3. It shows that for some field F , the value of F in the Cartesian grid is determined by performing a summation over n number of bins b that are within the radius of influence (ROI) of the center point of the grid cell, and d is the horizontal distance from the native bin to the center point of the cell. Vertical distance is neglected, as only the lowest elevation angle from the radars are included for comparison.

$$ROI = D * \tan \theta \quad (2.4)$$

The definition of ROI is found in Equation 2.4, where D is the horizontal distance from the grid cell to the radar and θ is the angular beamwidth. This completes the framework for comparing the radar datasets in this study.

2.2 Selection of Cases

Cases selected for this study were chosen entirely based on the pattern of motion and banding of the radar echoes. Radar mosaics for the study area were manually examined, beginning in 2014. When time intervals with echoes in the study area were observed, it was noted whether they trained over the same area, or were progressive. The former are classified as lake-effect driven events, while the latter are synoptically driven events. Also, a tabulation of critical level temperatures for the five lake-effect snow events selected is shown in Table 2.2, while the synoptic events are shown in Table 2.3. This shows ensures that all events were sufficiently below freezing, and dry snow was the predominant hydrometeor type.

Table 2.2: Critical level temperatures from radiosonde launched closest in time to the selected lake-effect snow events.

KBUF - Radiosonde	Radar Times	850mb T ($^{\circ}C$)	Lowest-Level T ($^{\circ}C$)
2014-01-23 00Z	0100-1000Z	-22.5	-14.9
2015-01-06 12Z	1200-1700Z	-20.1	-11.7
2015-02-14 12Z	1000-1400Z	-14.9	-6.9
2015-02-18 12Z	2100-2359Z	-17.3	-10.1
2016-02-10 12Z	1300-2359Z	-10.5	-2.7

2.3 Filtering Conditions

Several conditions were used to narrow down the selected sets to the best suited scans and individual gates for admission into the distance-weighting scheme.

2.3.1 Time Filter

Scan start times are compared between the radars, and if they are within four minutes of each other, the pair is admitted. For CWKR, there is a regular volume update frequency of ten minutes, while KBUF is variable based on the Volume Coverage Pattern (VCP) selected by the operator. The update frequency could be as short as every two minutes if the operator has activated Supplemental Adapative Intra-Volume Low-Level Scans (SAILS) mode.

Table 2.3: Critical level temperatures from radiosonde launched closest in time to the selected synoptic snow events.

KBUF - Radiosonde	Radar Times	850mb T ($^{\circ}$ C)	Lowest-Level T ($^{\circ}$ C)
2014-01-18 12Z	0600-0800Z	-11.3	-6.5
2015-01-07 12Z	0900-1100Z	-20.1	-11.7
2015-02-06 12Z	0900-1030Z	-16.3	-10.7
2016-01-06 12Z	0700-0900Z	-7.5	-0.7
2016-12-15 12Z	0920-1020Z	-20.3	-12.3

2.3.2 Gate Filters

2.4 Advanced Statistical Techniques

Scatter plots directly comparing grid cells produced by the distance-weighting scheme are used in this study. This section discusses how advanced statistical techniques were leveraged to derive the most information from these plots.

2.4.1 Kernel Density Estimation

Large radar datasets contain an immense amount of data; this requires the distillation of data to the greatest statistical significance. Scatter-plots containing on the order of 10^5 points become visually overwhelming. To solve this problem, a Kernel Density Estimation (KDE) technique is used. A 2-D KDE is essentially a way to estimate the joint probability density function of two random variables (Silverman 1986). Figure 2.3 demonstrates how this is achieved graphically, by first solving each individual kernel, then performing a summation. The units of the KDE can

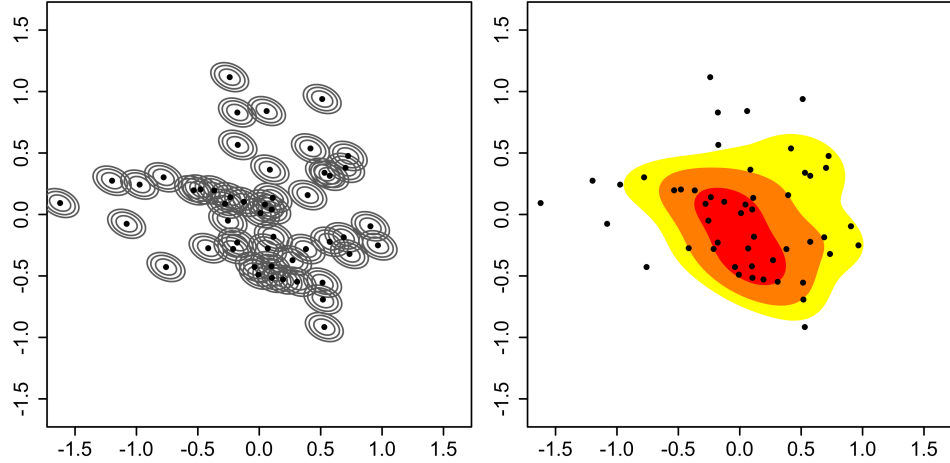


Figure 2.3: Illustration of the construction of 2D kernel density estimates. (Left) data points with individual kernels as grey dashed lines, (right) summed kernels = kernel density estimate.

be thought of as a likelihood ratio. Furthermore, the units are normalized by the matrix in Equation 2.5, where \mathbf{X} represents a 2-D histogram of the matched cells, n is the number of matched cells, and R is the histogram bin resolution, which matches the native data resolution.

$$\mathbf{N}_{i,j} = n * R^2 * \sqrt{\text{Det}|2\pi * \text{Cov}(\mathbf{X}_i, \mathbf{X}_j) * n^{-1/6}|} \quad (2.5)$$

2.4.2 Orthonormal Linear Regression

A hallmark of this study is the lack of ground truth. The sample sets compared, \mathbf{K} and \mathbf{C} , contain error prone, independent variables. Typically, scatter-plots compare an independent variable to a dependent variable. Instead of performing a standard linear regression between the variables, an orthonormal linear regression is used. This type of regression allows for error in both variables, by performing the least

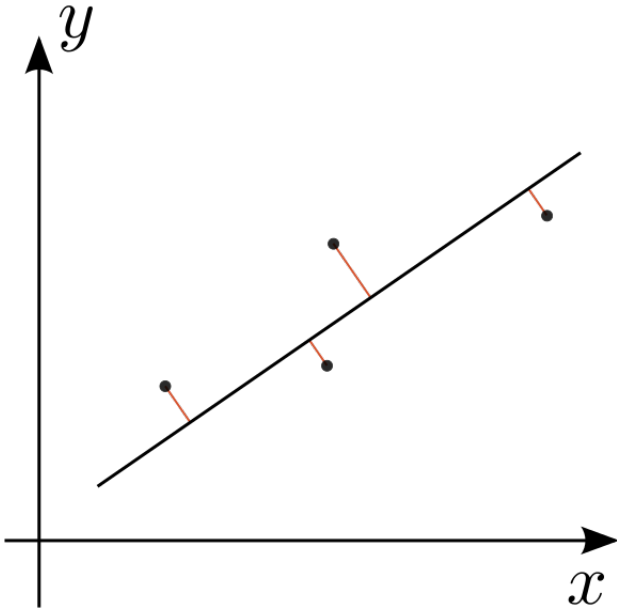


Figure 2.4: Demonstration of an Orthonormal Linear Regression

squares regression perpendicular to the initial fit instead of vertically (Markovsky and Huffel 2007). Figure 2.4 demonstrates this concept.

2.5 Z_{DR} Bias Estimation

Although it is not possible to check absolute calibration of Z_{eH} when comparing two radars, it is possible to verify Z_{DR} calibration due to relative nature of the quantity (Zrnic et al. 2006). While radars are regularly calibrated using internal calibration procedures, an external check is useful for monitoring the time-varying component of calibration. The typical process for calibration of Z_{DR} is pointing the antenna to zenith and performing “bird bath” scans during light rain events (Hubbert and Pratte 2006). The Z_{DR} in light rain is expected to be 0 dB, therefore any offset from this is considered a bias; The signal processor subtracts out this bias to achieve the final output. Due to mechanical constraints, NEXRAD radars are unable to perform

this procedure, but CWKR is (citation needed). NEXRAD radars disseminate a product which contains an estimate of Z_{DR} bias using the intrinsic properties of dry snow Zittel et al. (2015). The daily published offset will be used to adjust Z_{DR} values obtained from KBUF to diagnose any bias at CWKR.

3 Chapter Three

3.1 Event Comparisons

Now, we consider each of the selected events individually, demonstrating that the events were classified correctly, and breaking down the results from each case. Although it is nearly impossible to extricate lake influence from synoptically classified events, synoptic-scale ascent is considered the characterizing factor. Descriptions of the synoptic pattern during each event are given without reference; For reference, see Appendix A for the 500mb Geopotential Heights, Skew-T charts, and Sounding Climatology utilized. These descriptions are ancillary to the study and are provided to demonstrate a variety of patterns are represented.

3.1.1 18 January 2014 - Synoptic

In this event, a weak shortwave is approaching Southern Ontario as it rounds the base of a longwave trough centered over the Eastern US. With the study area in the attendant region of upper-level divergence, and a moist column present through 500mb, scattered snow showers form ahead of the shortwave. Figure 3.1 depicts similiar cellular patterns between radars in the time-averaged Z_{eH} field. In contrast, the Z_{DR} comparison in Figure 3.2 shows that although the fields are similiar in their anisotropy, the spatial matching between the two is tenuous everywhere but in the heaviest showers.

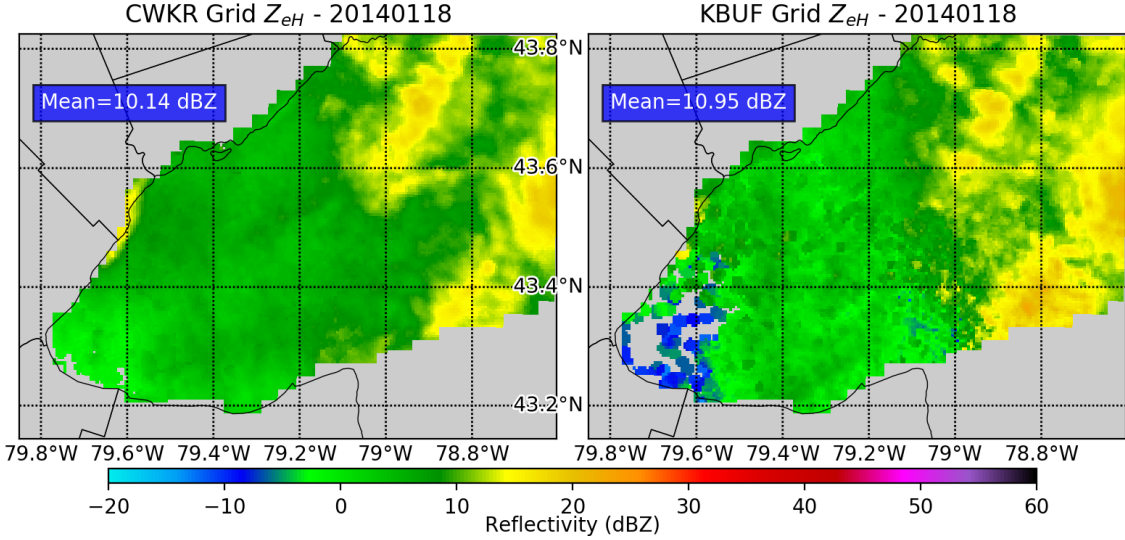


Figure 3.1: Gridded Z_{eH} comparison for 18 January 2014. Time-average of all admitted scans.

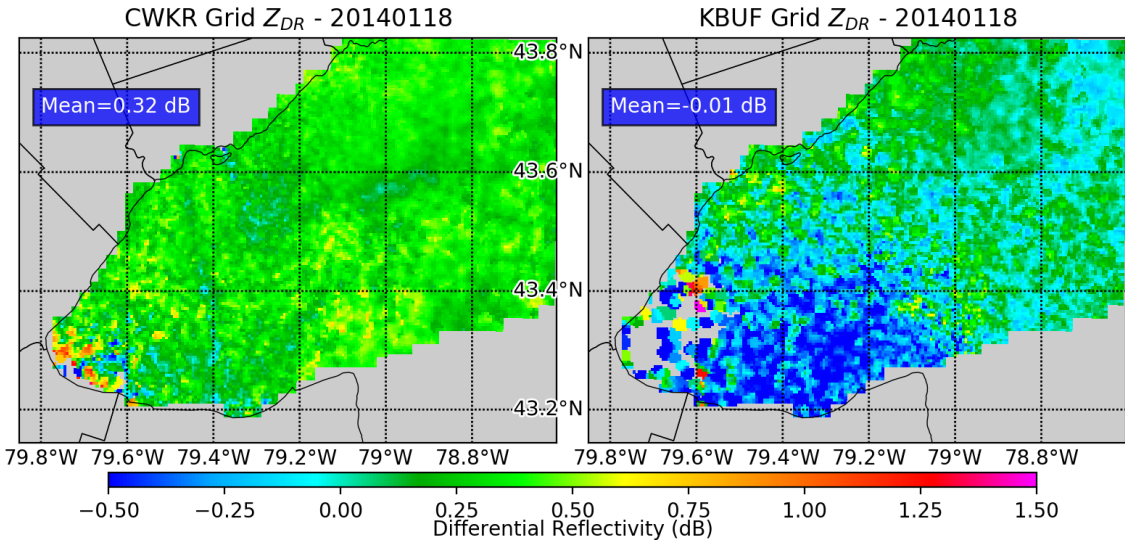


Figure 3.2: Gridded Z_{DR} comparison for 18 January 2014. Time-average of all admitted scans.

To investigate further, we examine a scatter-plot directly comparing matched values between radars. Artifacts are present in both moments in Figure 3.3, indicated by evenly spaced vertical lines; these indicate an anomaly originating from the axis of which they are normal to. For Z_{eH} , Figure 3.3a shows that artifacts are no longer present for values greater than 15 dBZ, which indicates that a stronger weather signal leads to better matching. On the contrary, Figure 3.3b shows that for Z_{DR} , artifacts are present throughout. Also, the distribution of Z_{DR} is unimodal.

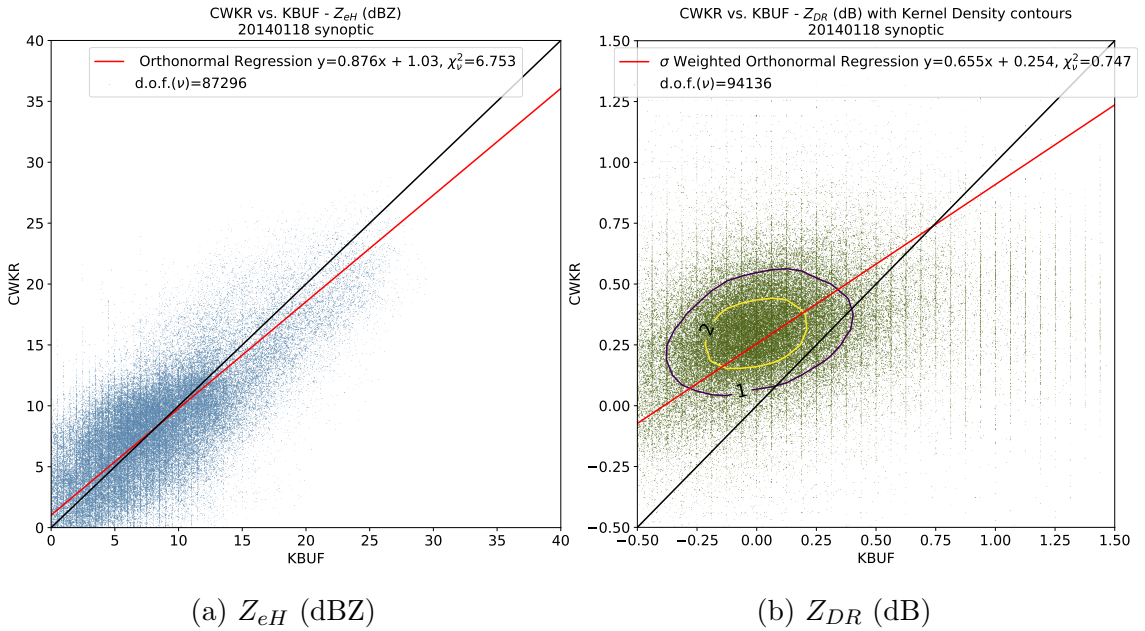


Figure 3.3: Direct comparisons for 18 January 2014. Dataset includes all admitted grid cells.

It is still possible to extract a signal from the noise though, by excluding data points with a normalized kernel density less than two. These points are used to resolve the bias present in Z_{DR} , as suggested by the comparisons. Figure 3.4 gives an estimate of the bias at CWKR by using this method and the known bias at KBUF as provided by the NEXRAD External Target Bias Estimation technique.

This method yields a median of -0.095 dB for the bias at CWKR, which when considered with the error threshold of ± 0.1 dB, indicates no discernible bias.

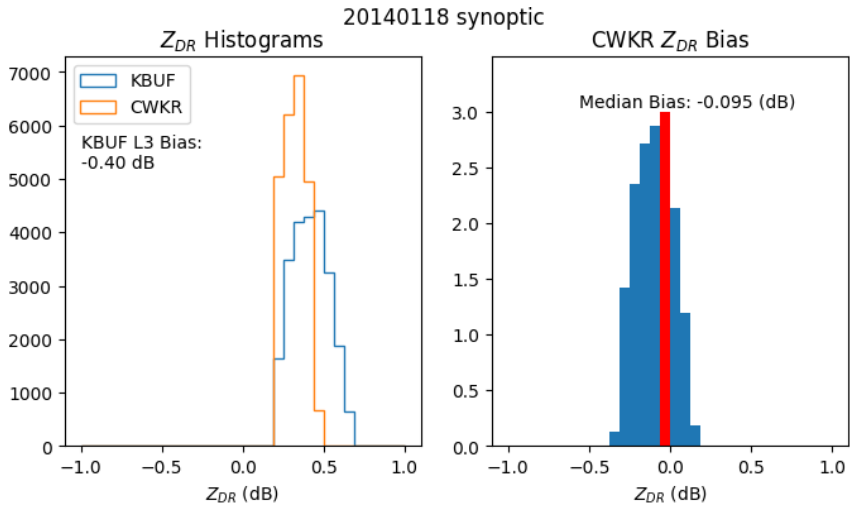


Figure 3.4: Histograms of Z_{DR} (left), Z_{DR} bias at CWKR, determined by subtracting the gridded, bias adjusted Z_{DR} at KBUF from the Z_{DR} at CWKR. Both datasets exclude matched points with $KDE < 2$.

3.1.2 23 January 2014 - Lake-Effect

A positively tilted longwave trough dominates the eastern third of Canada during this event, with NW winds at 850mb and SW winds at the surface. This light yet convergent flow yields the single, heavy band depicted in Figure 3.5, colloquially referred to as “tea-kettle” lake-effect snow. There is also a background stream of very light lake-effect snow impinging from Lake Erie. Spatial banding patterns of the lake-effect snow in the time-averaged Z_{eH} fields as compared between the radars are remarkably similar. The difference between the grid mean values are within only 0.13 dBZ. In contrast, the Z_{DR} comparison indicates that although the fields are similar in their anisotropy, the spatial matching between the two

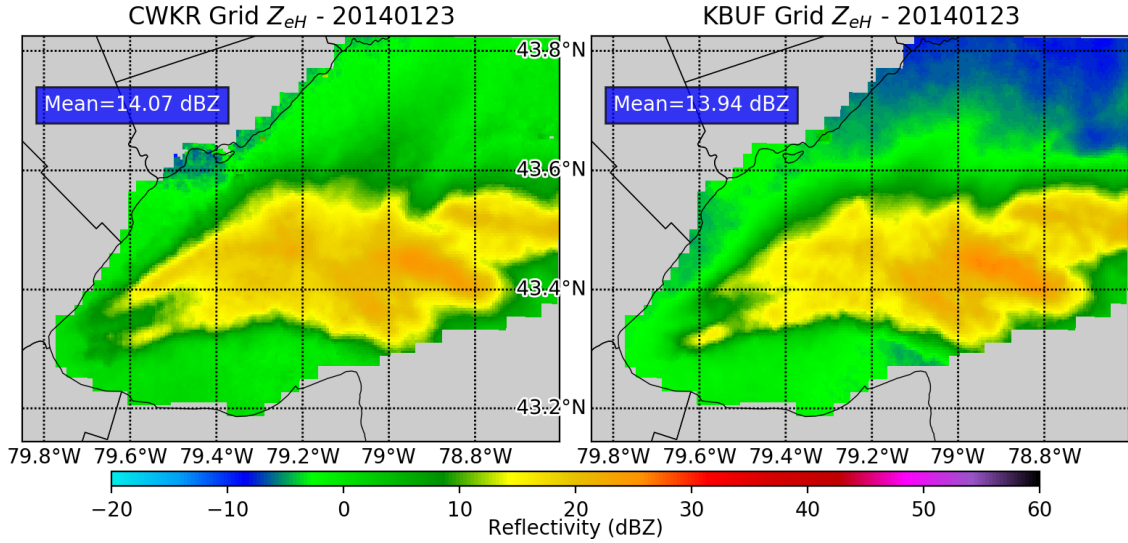


Figure 3.5: Gridded Z_{eH} comparison for 23 January 2014. Time-average of all admitted scans.

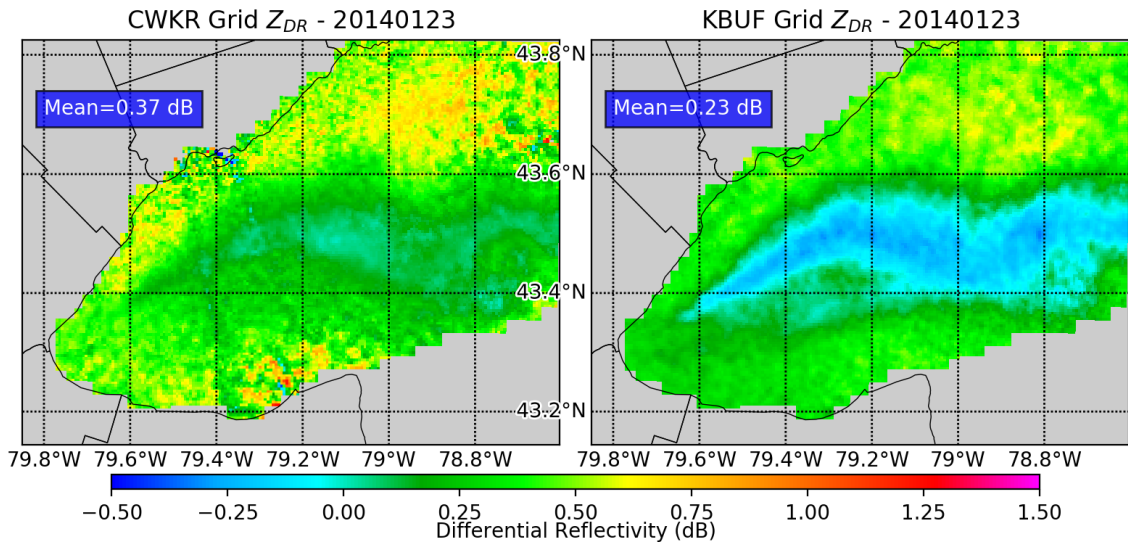


Figure 3.6: Gridded Z_{DR} comparison for 23 January 2014. Time-average of all admitted scans.

is tenuous everywhere but in the heaviest showers. An anisotropic pattern is also imparted on the Z_{DR} fields by the light snow from Lake Erie, evident in Figure 3.6. The scatter-plot in Figure 3.7a shows an analysis free of artifacts, and good agreement on average between radars. Although the agreement in Z_{eH} between radars as indicated by the orthonormal regression is acceptable, the chi-square statistic indicates a high error variance. A slightly bi-modal distribution of Z_{DR} is shown in Figure 3.7a, with the main peak near 0 dB and a secondary peak near 0.5 dB, with artifacts much more prevalent near the secondary peak. Both analysis methods have indicated a bias in Z_{DR} , so the kernel density method for estimating bias is used. Figure 3.8 shows an estimate of the bias at CWKR, with a median value of -0.055 dB. Once again, no discernible bias exists outside of the error threshold of ± 0.1 dB for this event.

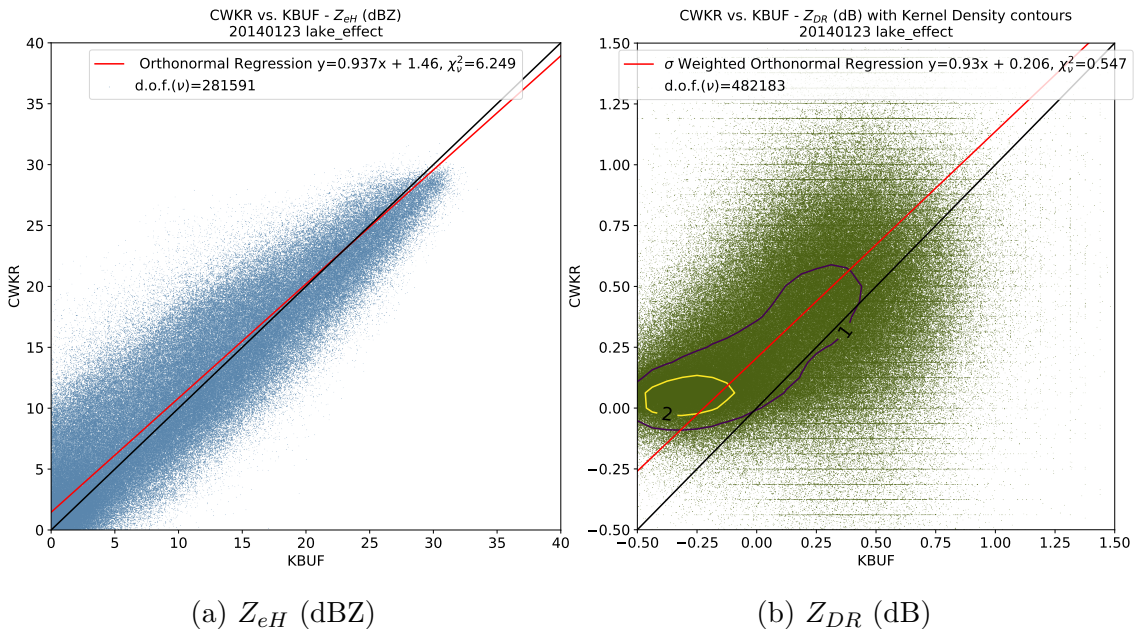


Figure 3.7: Direct comparisons for 23 January 2014. Dataset includes all admitted grid cells.

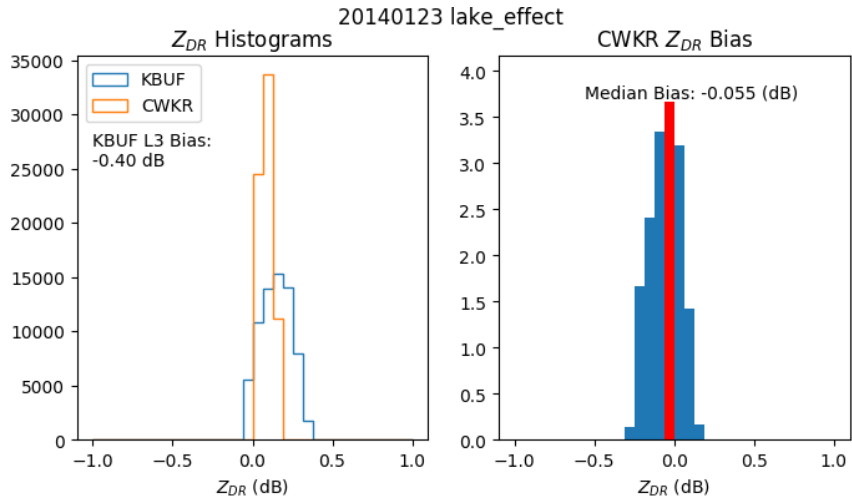


Figure 3.8: Histograms of Z_{DR} (left), Z_{DR} bias at CWKR, determined by subtracting the gridded, bias adjusted Z_{DR} at KBUF from the Z_{DR} at CWKR. Both datasets exclude matched points with $KDE < 2$.

3.1.3 1 February 2014 - Synoptic

This event is characterized by strong SW flow aloft, with above average moisture content. This leads to widespread stratiform snow, with an eventual transition to rain outside of the time interval selected. A large swath of steady snow is depicted by the time-averaged Z_{eH} in Figure 3.9. Furthermore, Figure 3.10 shows smoother Z_{DR} fields as compared with other events, which confirms the stratiform nature of the precipitation. Next, Figure 3.11a indicates very good agreement in Z_{eH} with low error variance, while Figure 3.11b shows a very dense uni-modal, biased kernel for Z_{DR} . The histogram in Figure 3.12 reveals that the anomalous bias between the radars is indicative of a Z_{DR} bias at CWKR, with a value of 0.217 dB. The source of this bias will be discussed in the next chapter.

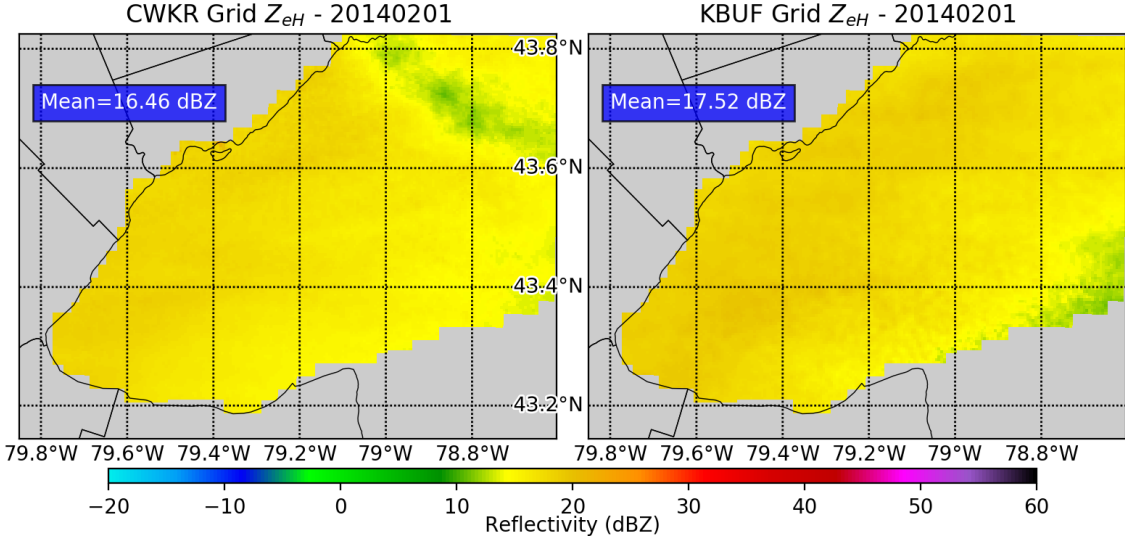


Figure 3.9: Gridded Z_{eH} comparison for 1 February 2014. Time-average of all admitted scans.

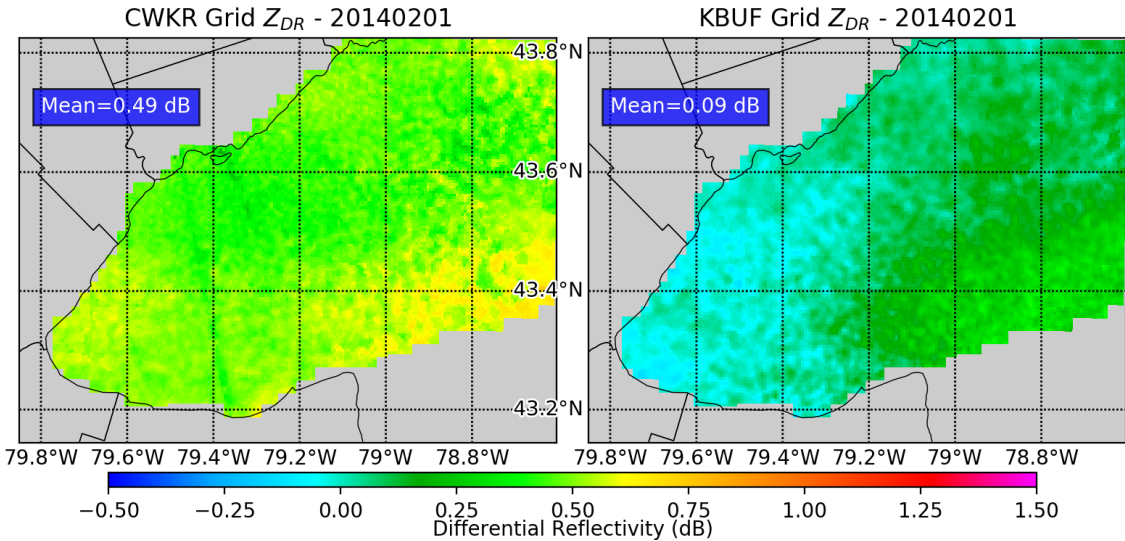


Figure 3.10: Gridded Z_{DR} comparison for 1 February 2014. Time-average of all admitted scans.

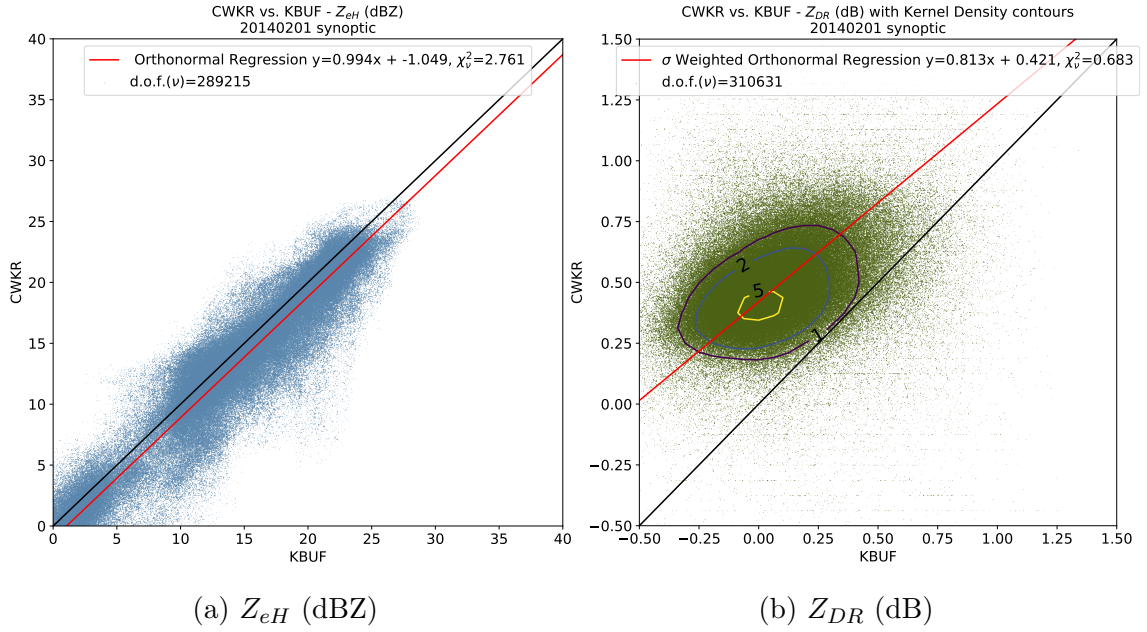


Figure 3.11: Direct comparisons for 1 February 2014. Dataset includes all admitted grid cells.

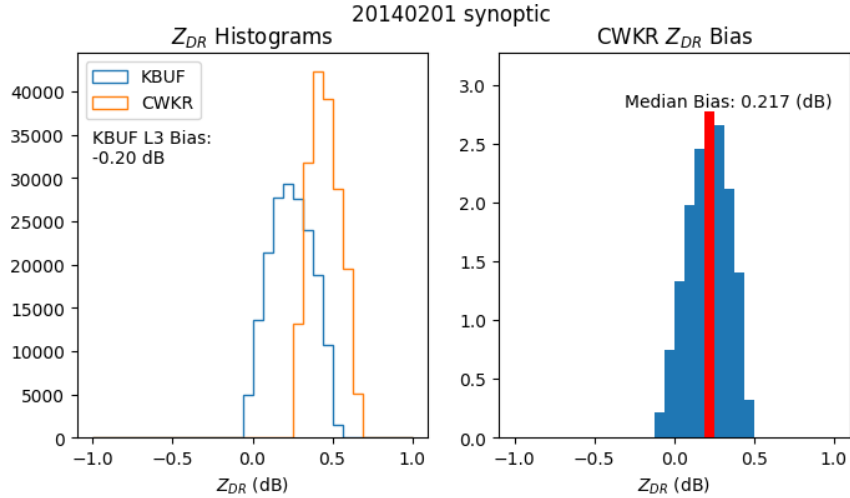


Figure 3.12: Histograms of Z_{DR} (left), Z_{DR} bias at CWKR, determined by subtracting the gridded, bias adjusted Z_{DR} at KBUF from the Z_{DR} at CWKR. Both datasets exclude matched points with KDE < 2.

3.1.4 6 January 2015 - Lake-Effect

A highly zonal, NW flow aloft is present in this case, a typical pattern for lake-effect snow across the Great Lakes region. Anemic in radar appearance, a lake-effect band develops in the light winds near the surface; this case could be characterized as a weak “tea-kettle” event. Figure 3.13 depicts stationary banding in the time-averaged Z_{eH} . Of note is that CWKR observes more of the finer scale features as compared with KBUF, also evidenced by the +2.9 dBZ difference in Z_{eH} mean.

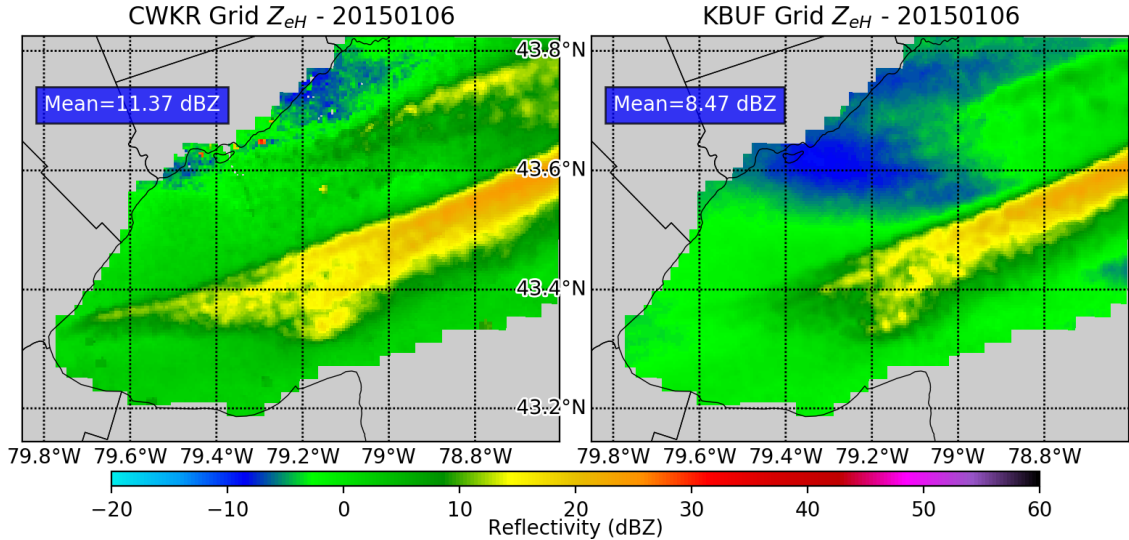


Figure 3.13: Gridded Z_{eH} comparison for 6 January 2015. Time-average of all admitted scans.

This case stands out from the rest in terms of Z_{DR} , as the fields are very similar and unbiased as shown in Figure 3.14. The scatter-plot in Figure 3.15a confirms what is shown in the gridded Z_{eH} , with values skewed higher for CWKR. Figure 3.15b shows a bi-modal distribution for Z_{DR} , with the main peak around 0.5 dB and a secondary peak near 0 dB. The histogram in Figure 3.16 confirms the observed unbiased Z_{DR} , with a near zero median value of 0.003 dB.

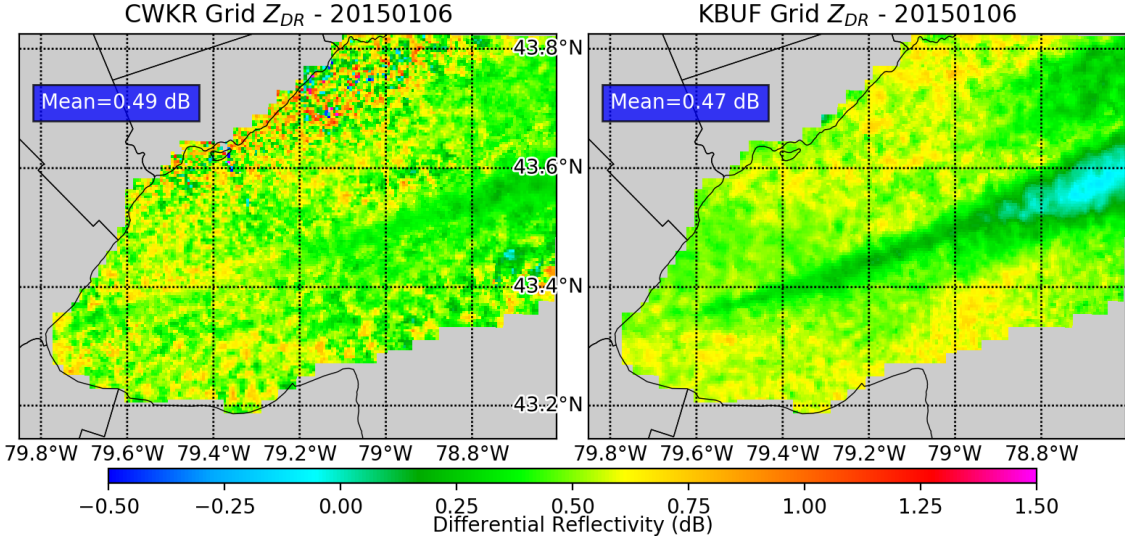


Figure 3.14: Gridded Z_{DR} comparison for 6 January 2015. Time-average of all admitted scans.

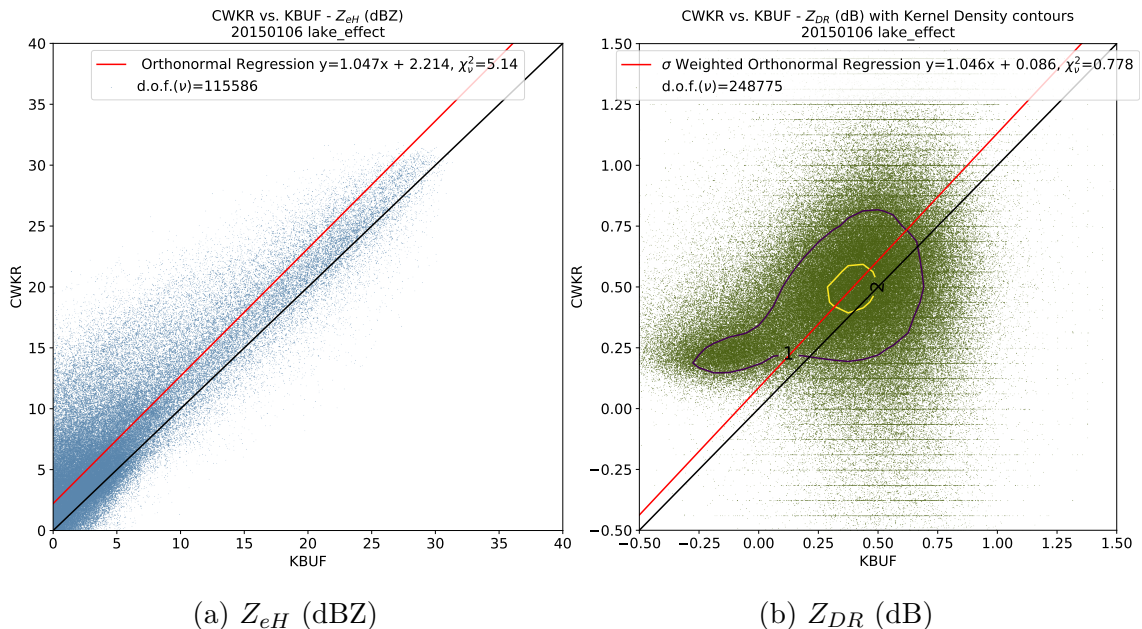


Figure 3.15: Direct comparisons for 6 January 2015. Dataset includes all admitted grid cells.

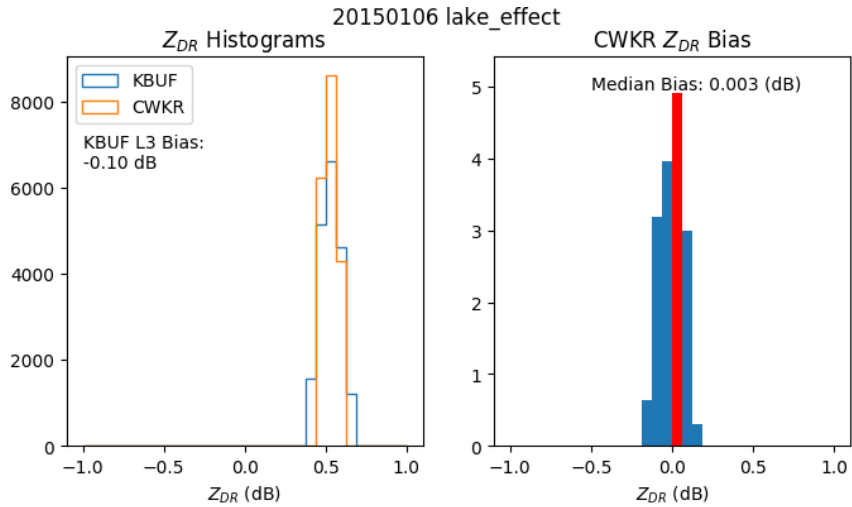


Figure 3.16: Histograms of Z_{DR} (left), Z_{DR} bias at CWKR, determined by subtracting the gridded, bias adjusted Z_{DR} at KBUF from the Z_{DR} at CWKR. Both datasets exclude matched points with $KDE < 2$.

3.1.5 7 January 2015 - Synoptic

Less than 24 hours after the previous event, the zonal flow has buckled and a strong shortwave is overhead Southern Ontario. Radar animations indicate a frontally forced band of snow showers. Figure 3.17 shows the solid band of snow progressed from mid-lake southward, with similar depictions of Z_{eH} between radars. Inspection of the scatter-plot in Figure 3.19a indicates good agreement with reasonable error variance, while Figure 3.19b shows a uni-modal distribution of Z_{DR} with a relatively dense kernel. Meanwhile, Figure 3.18 shows two anisotropic fields, especially noisy in areas of light returns. Estimating the bias at CWKR, the histogram in Figure 3.20 gives a median value of -0.040 dB. This indicates that no discernible bias exists outside of the error threshold of ± 0.1 dB for this event.

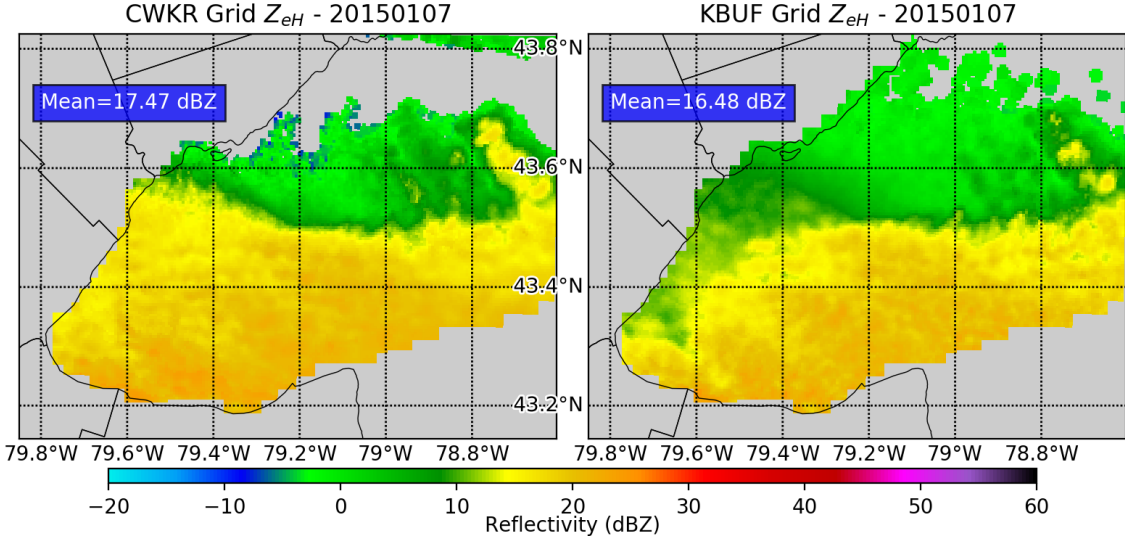


Figure 3.17: Gridded Z_{eH} comparison for 7 January 2015. Time-average of all admitted scans.

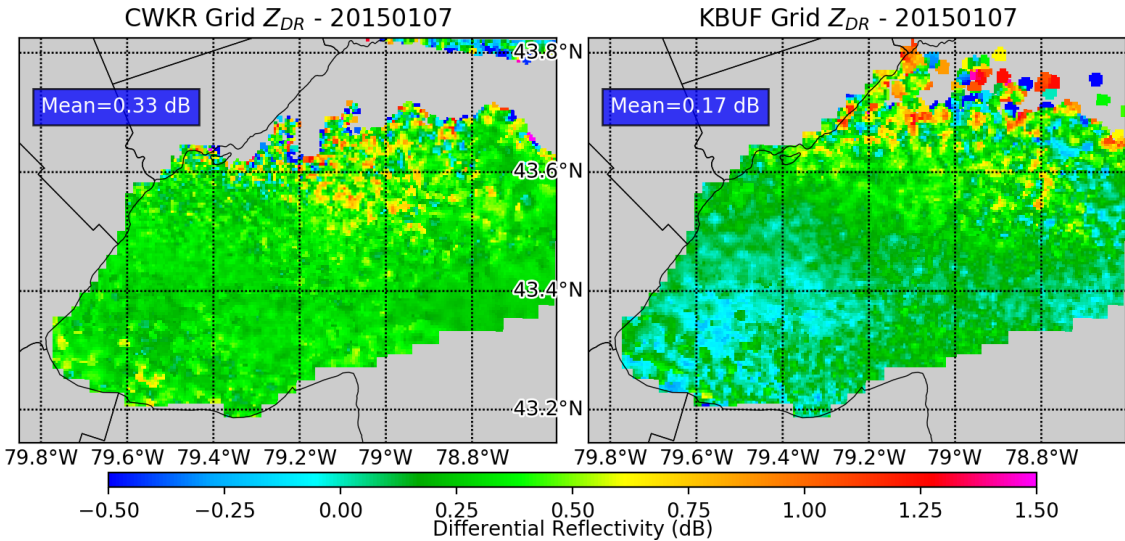


Figure 3.18: Gridded Z_{DR} comparison for 7 January 2015. Time-average of all admitted scans.

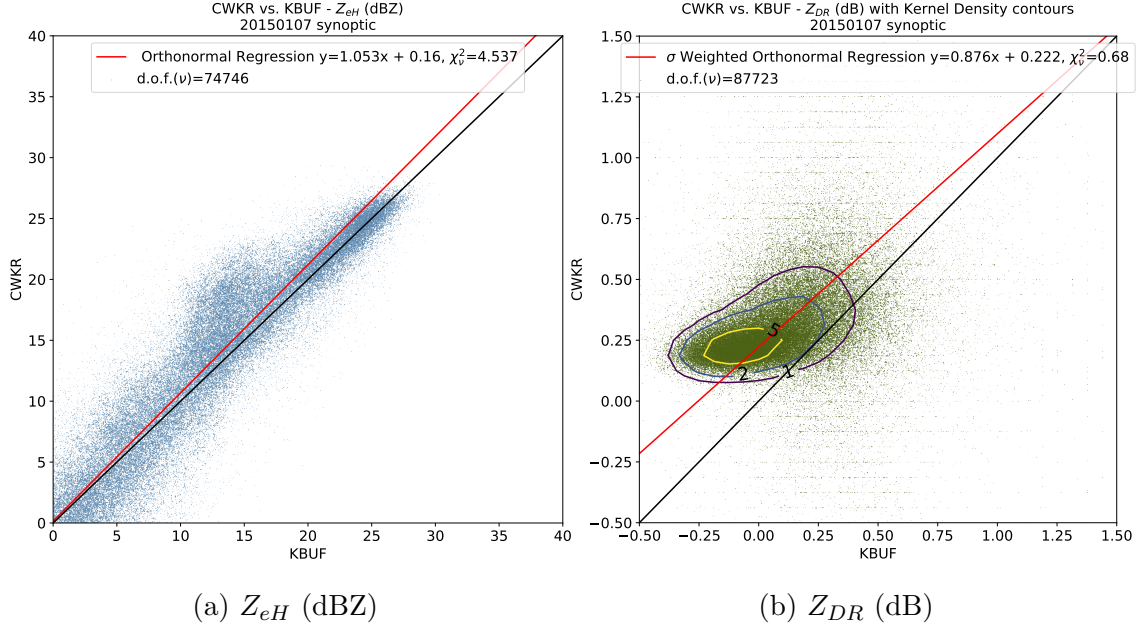


Figure 3.19: Direct comparisons for 7 January 2015. Dataset includes all admitted grid cells.

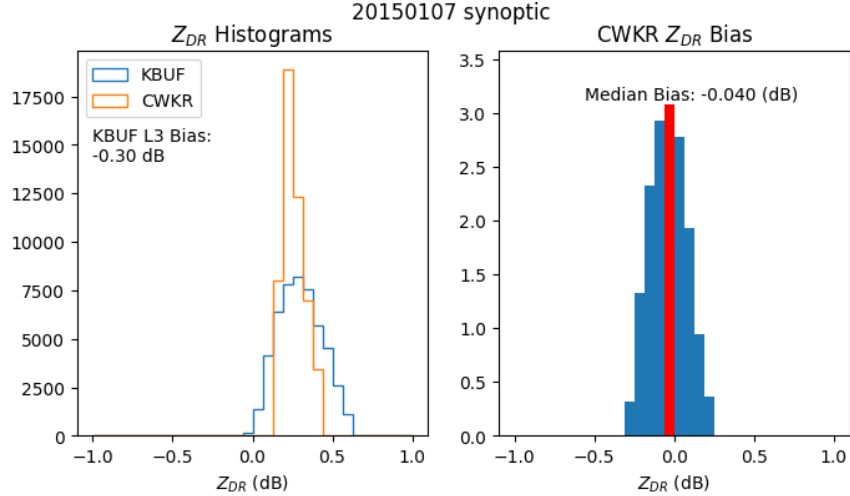


Figure 3.20: Histograms of Z_{DR} (left), Z_{DR} bias at CWKR, determined by subtracting the gridded, bias adjusted Z_{DR} at KBUF from the Z_{DR} at CWKR. Both datasets exclude matched points with KDE < 2.

3.1.6 6 February 2015 - Synoptic

With a strong ridge centered over the SW US, Southern Ontario is on the backside of progressive shortwave, with a frontal passage occurring once again. A broad swath of snow is depicted by the time-averaged Z_{eH} fields in Figure 3.21, with the CWKR mean value 2 dBZ higher than KBUF.

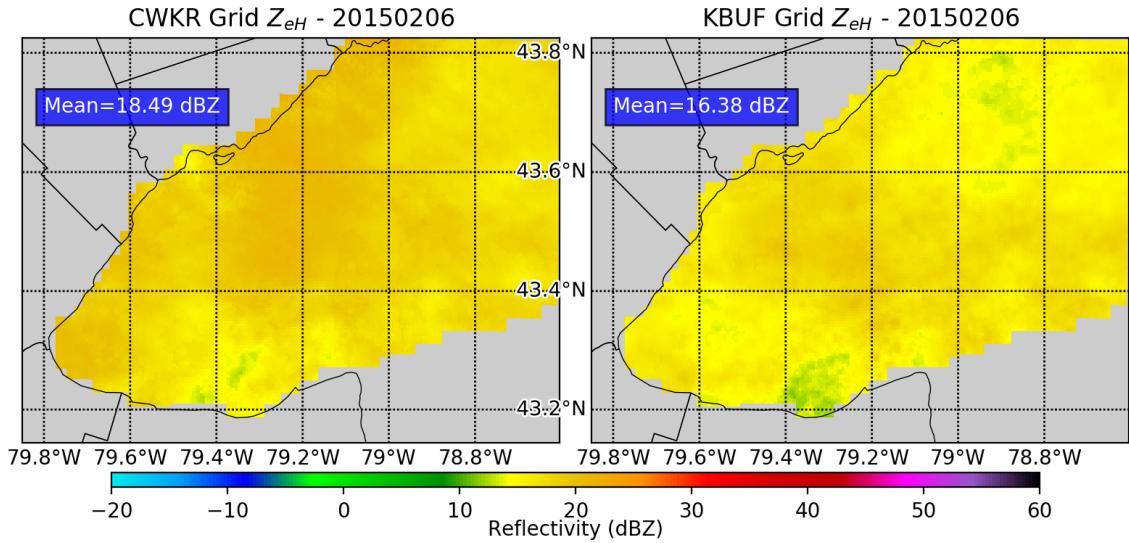


Figure 3.21: Gridded Z_{eH} comparison for 6 February 2015. Time-average of all admitted scans.

Comparing Z_{DR} as shown in Figure 3.22, the fields are similar but slightly biased. Beam blockages are noted at CWKR as indicated by the stripes in the NE section of grid. Next to the scatter-plots, with Figure 3.23 indicating a high frequency of points between 15-25 dBZ, a preferred range for comparing Z_{DR} values. Also of note is the high error variance of 9.773 . Figure 3.23b shows a dense, symmetric kernel with an ill-fitted regression. Proceeding on to the histograms in Figure 3.24, a median bias of 0.283 dB at CWKR is estimated. The source of the bias will be discussed in the next chapter.

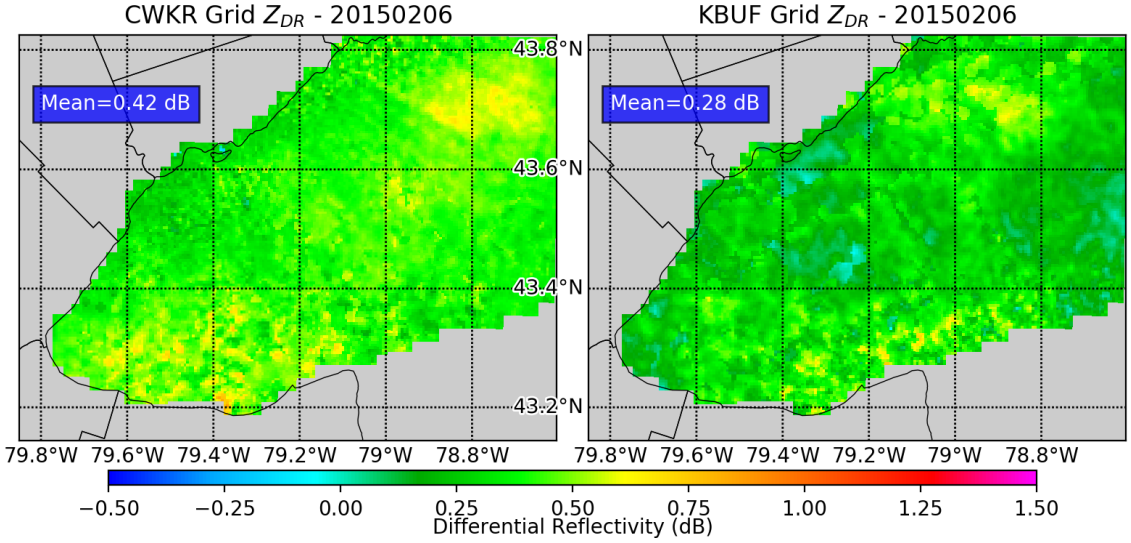


Figure 3.22: Gridded Z_{DR} comparison for 6 February 2015. Time-average of all admitted scans.

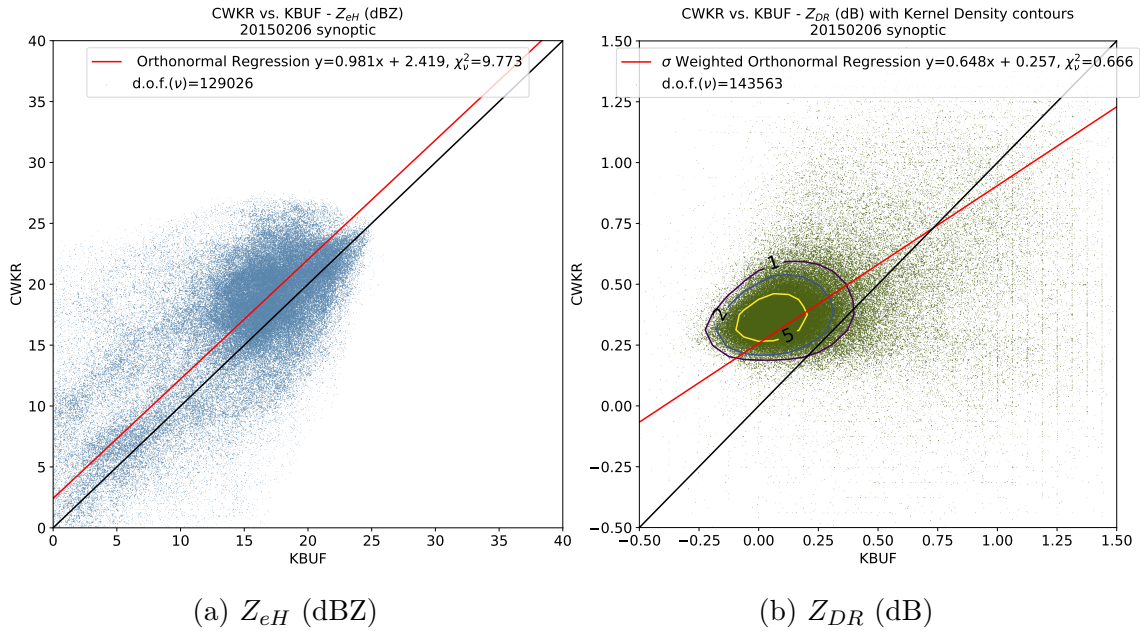


Figure 3.23: Direct comparisons for 6 February 2015. Dataset includes all admitted grid cells.

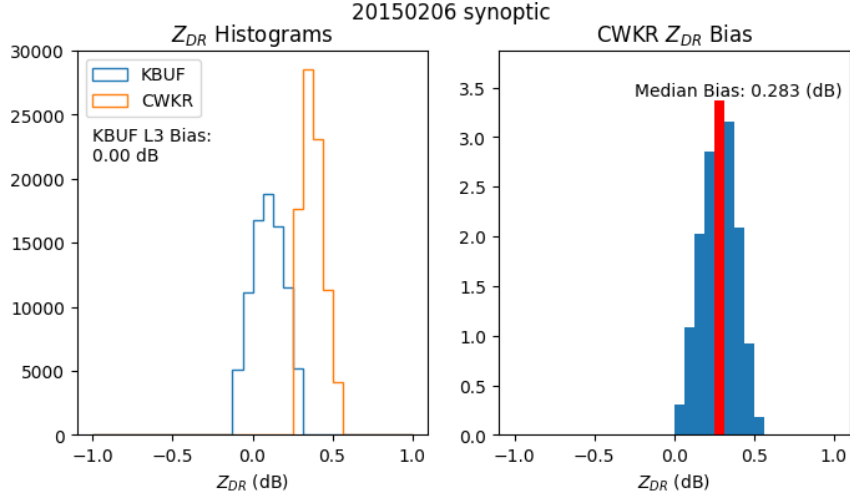


Figure 3.24: Histograms of Z_{DR} (left), Z_{DR} bias at CWKR, determined by subtracting the gridded, bias adjusted Z_{DR} at KBUF from the Z_{DR} at CWKR. Both datasets exclude matched points with $KDE < 2$.

3.1.7 14 February 2015 - Lake-Effect

While Southern Ontario is bracing for the impact of a bowling-ball like lobe of the polar vortex, strong W to SW flow from the surface to 850mb allows for a prolonged period of lake-effect snow over the lake. From Figure 3.25, we see again that CWKR resolves the convective scale features of the snow squalls better than KBUF. Horizontal convective rolls are clearly depicted by CWKR, whereas they become muddled by KBUF. Figure 3.26 shows similar patterns of Z_{DR} , but a large bias exists. The Z_{eH} scatter-plot in Figure 3.27 shows a dense clustering of points for low values, becoming increasingly skewed towards CWKR as they increase. For Z_{DR} , the variance-weighted regression achieves a near perfect reduced chi statistic (χ^2_ν) of 0.968. The histogram in Figure 3.28 indicates an anomalous bias for this event, with a median value of 0.377 dB.

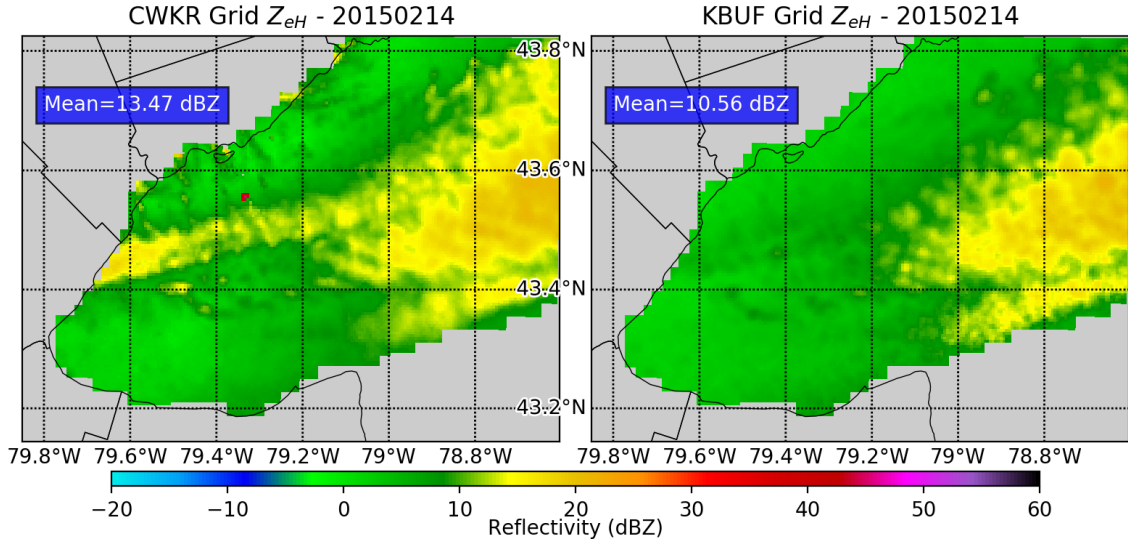


Figure 3.25: Gridded Z_{eH} comparison for 14 February 2015. Time-average of all admitted scans.

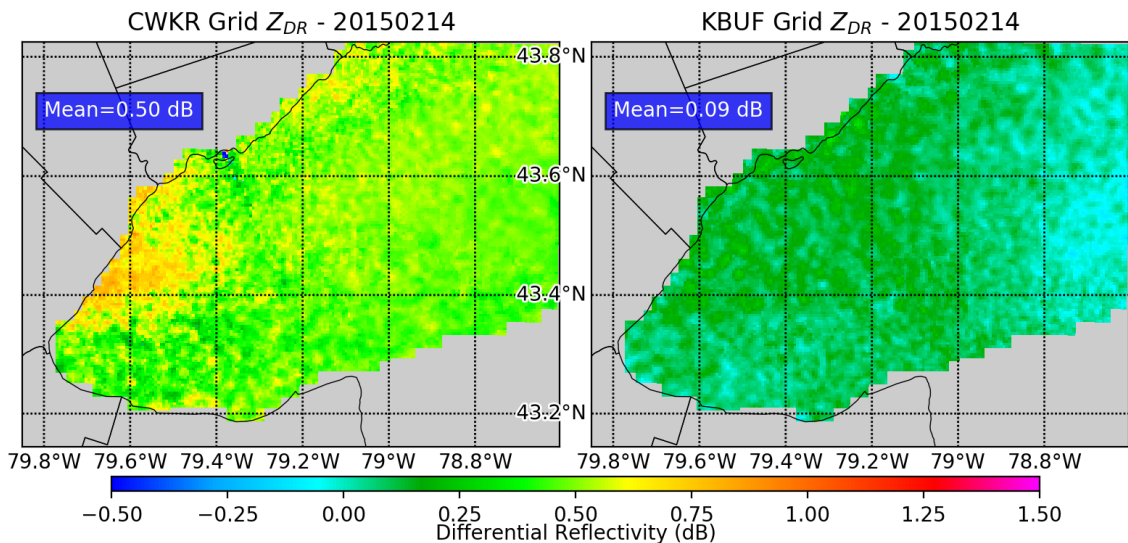


Figure 3.26: Gridded Z_{DR} comparison for 14 February 2015. Time-average of all admitted scans.

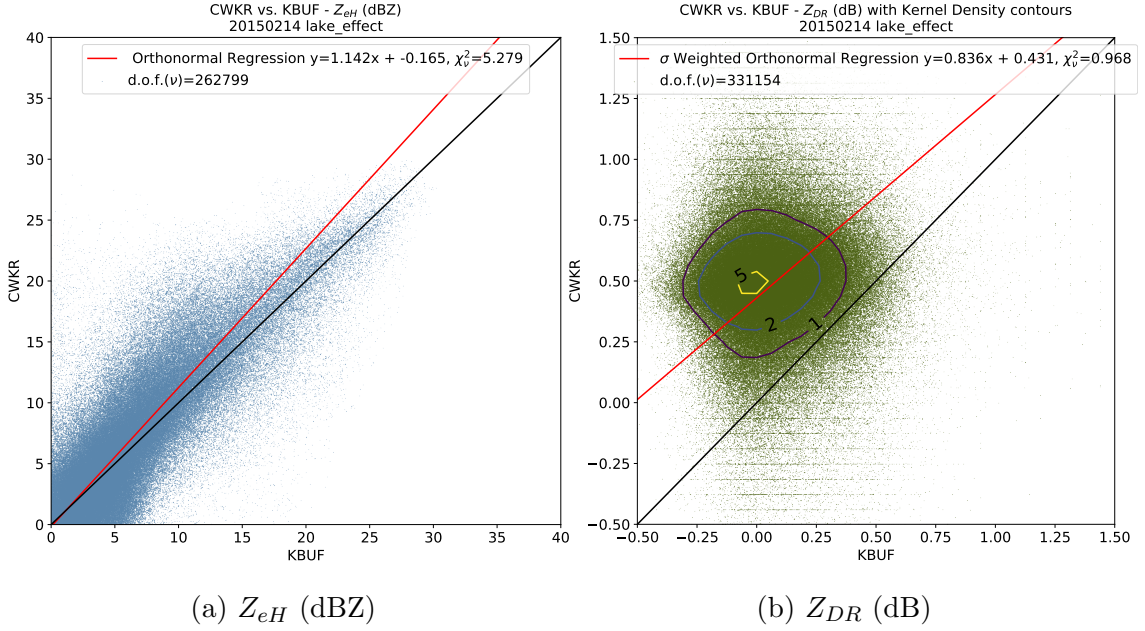


Figure 3.27: Direct comparisons for 14 February 2015. Dataset includes all admitted grid cells.

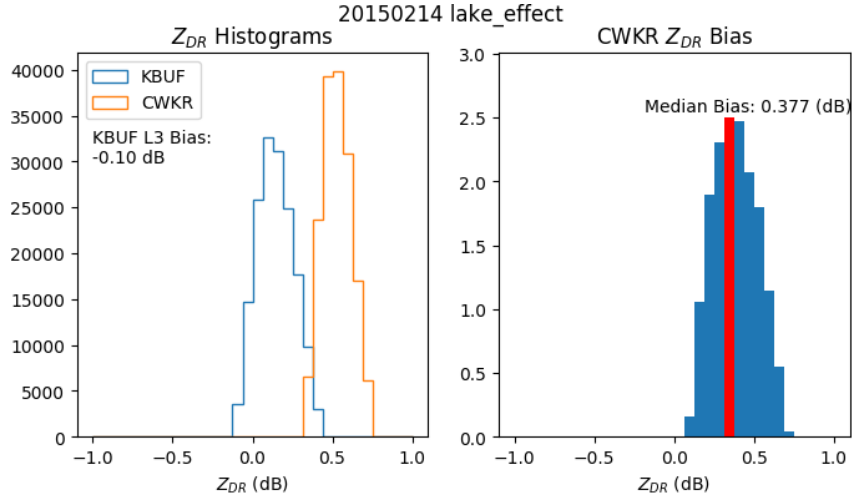


Figure 3.28: Histograms of Z_{DR} (left), Z_{DR} bias at CWKR, determined by subtracting the gridded, bias adjusted Z_{DR} at KBUF from the Z_{DR} at CWKR. Both datasets exclude matched points with KDE < 2.

3.1.8 18 February 2015 - Lake-Effect

Four days later, The polar vortex has arrived in earnest for this event, with the 500 dm isoheight at 500mb nearing as far south as Windsor, ON. The cold airmass allows for the development of an intense lake-effect snow band, the strongest of all the lake-effect cases as indicated by the Z_{eH} means in Figure 3.29. Next, Figure 3.30 shows similar band structure as compared between radars, with a bias evident. A orthonormal fit with decent agreement between radars is shown in Figure 3.31a, with the values biased towards CWKR all along the line. In Figure 3.31b, a unique bi-modal distribution of Z_{DR} is shown, with two peaks equal in magnitude around 0.50 dB and 0.75 dB. The histogram in Figure 3.32 also depicts this bi-modal distribution of Z_{DR} , and gives an estimate median value of 0.296 dB. The source of the bias will be discussed in the next chapter.

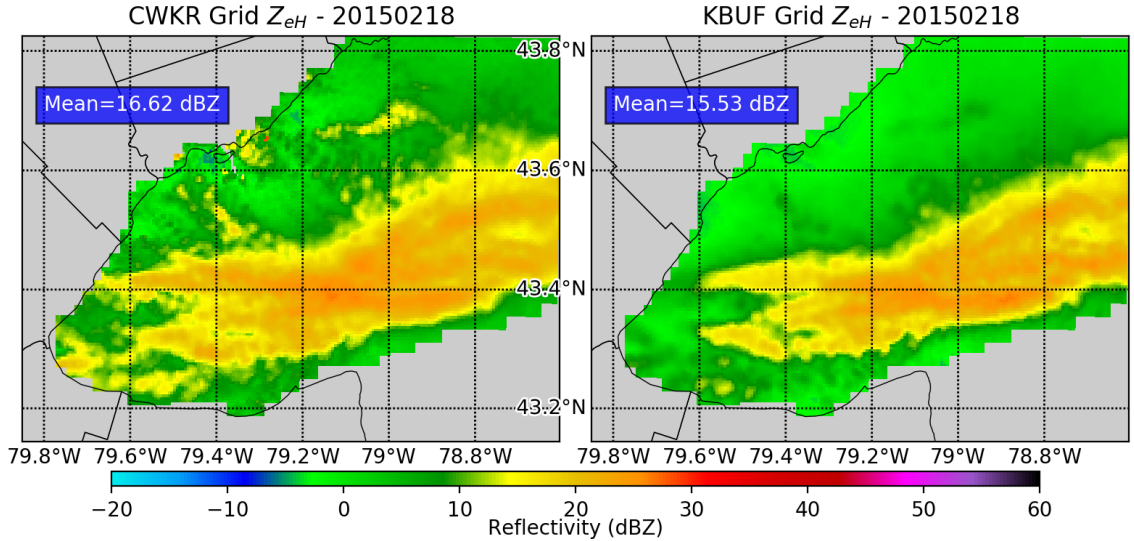


Figure 3.29: Gridded Z_{eH} comparison for 18 February 2015. Time-average of all admitted scans.

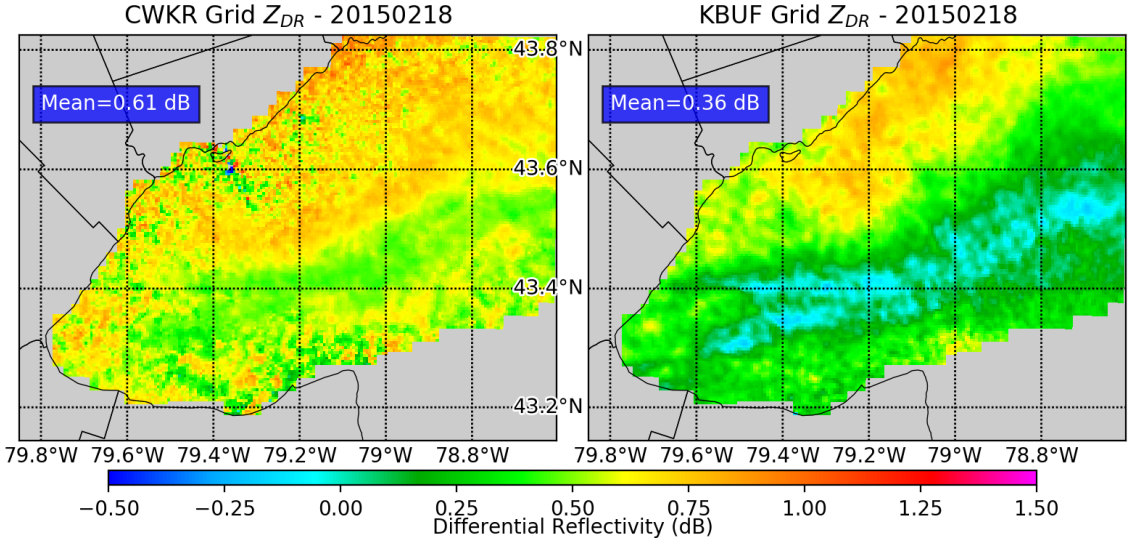


Figure 3.30: Gridded Z_{DR} comparison for 18 February 2015. Time-average of all admitted scans.

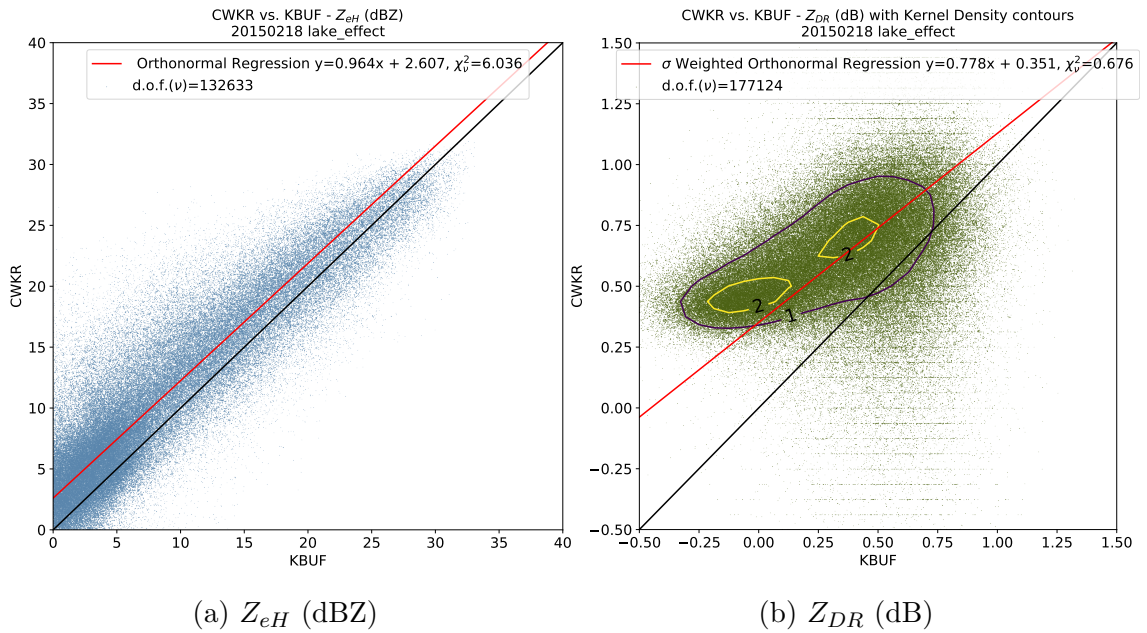


Figure 3.31: Direct comparisons for 18 February 2015. Dataset includes all admitted grid cells.

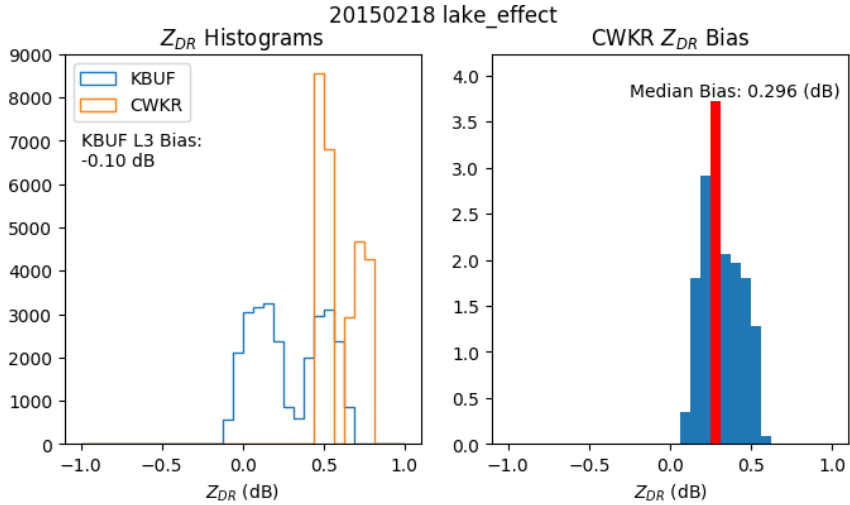


Figure 3.32: Histograms of Z_{DR} (left), Z_{DR} bias at CWKR, determined by subtracting the gridded, bias adjusted Z_{DR} at KBUF from the Z_{DR} at CWKR. Both datasets exclude matched points with $KDE < 2$.

3.1.9 10 February 2016 - Lake-Effect

The 500mb ridge axis is centered to the south of Southern Ontario in the Appalachians, with WNW flow aloft during this event. With a slight amount of pre existing instability augmenting the lake induced instabilities, a healthy band of lake-effect snow forms on the southern end of the lake. KBUF observes higher values of Z_{DR} in this band on the southern edge of the lake, as shown in Figure 3.33. This is likely due to the CWKR beam overshooting the shallow convection while the KBUF beam is lower in height. The intensity of the band overcomes the degraded signal strength due beam blockages at CWKR, evident in Z_{DR} on the western end of the band in Figure 3.34.

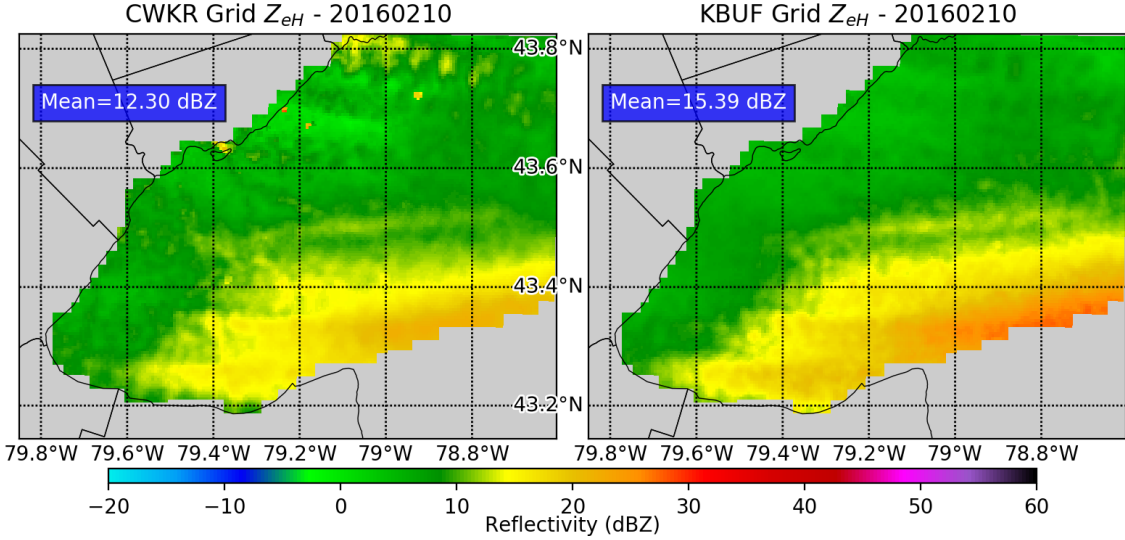


Figure 3.33: Gridded Z_{eH} comparison for 10 February 2016. Time-average of all admitted scans.

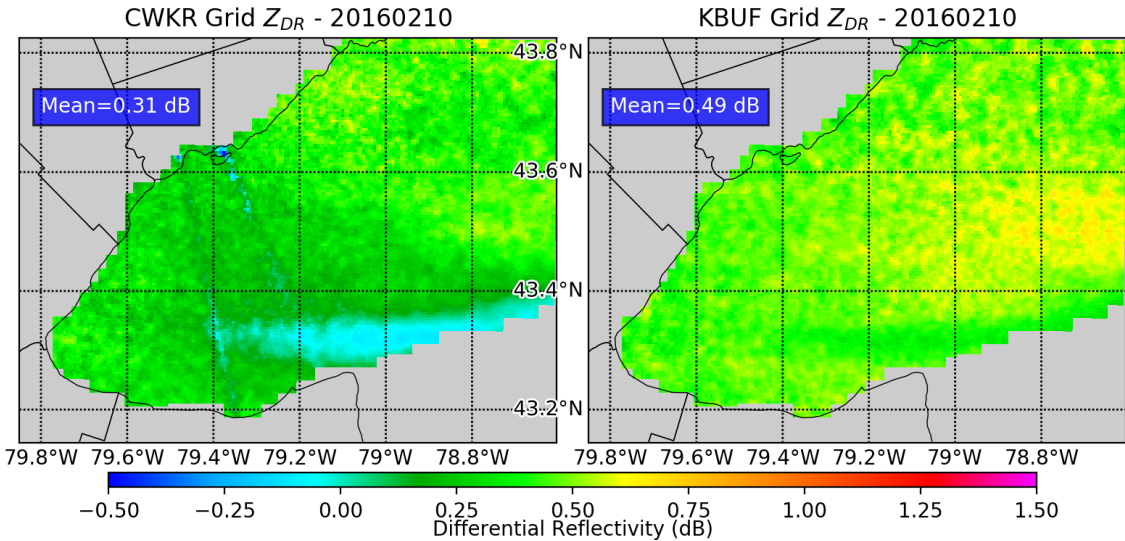


Figure 3.34: Gridded Z_{DR} comparison for 10 February 2016. Time-average of all admitted scans.

Due to the long duration of this case, the large sample of matched points was obtained from this case. Figure 3.35a shows that matched Z_{eH} values tends higher towards KBUF as they increase. Next, Figure 3.35b demonstrates the value of the kernel density estimate, as its impossible to visually analyze a scatter-plot with nearly a million points. The kernel extracted from the data is small, but information rich. Figure 3.36 leverages this information to show that the median Z_{DR} at CWKR is -0.055 dB, indicating no discernible bias exists outside of the error threshold of ± 0.1 dB for this event.

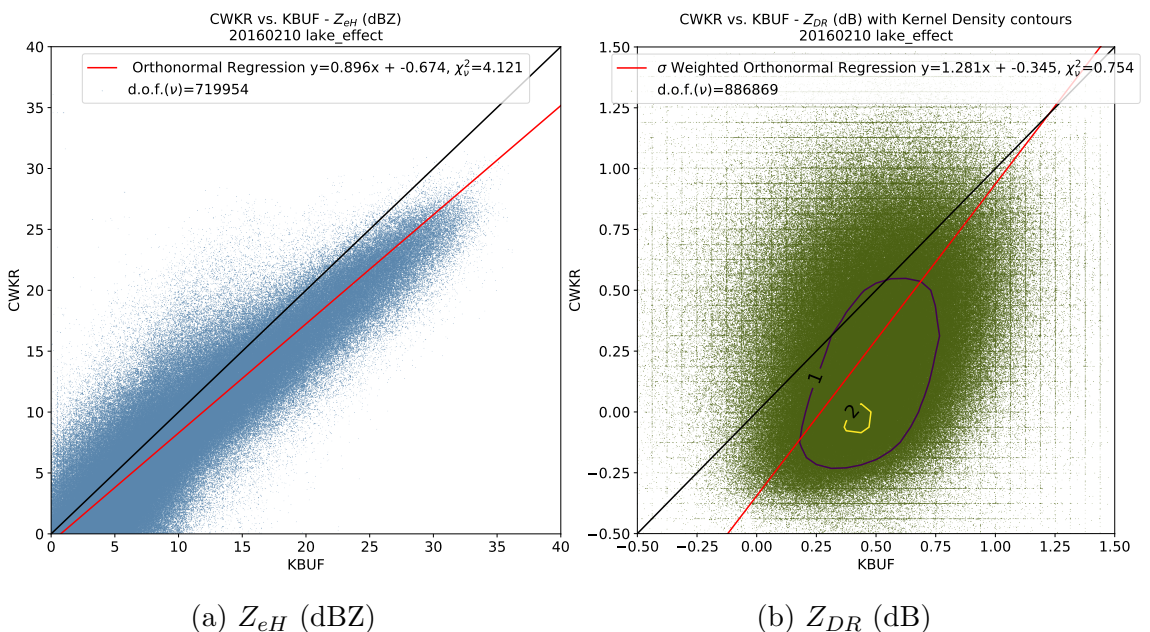


Figure 3.35: Direct comparisons for 10 February 2016. Dataset includes all admitted grid cells.

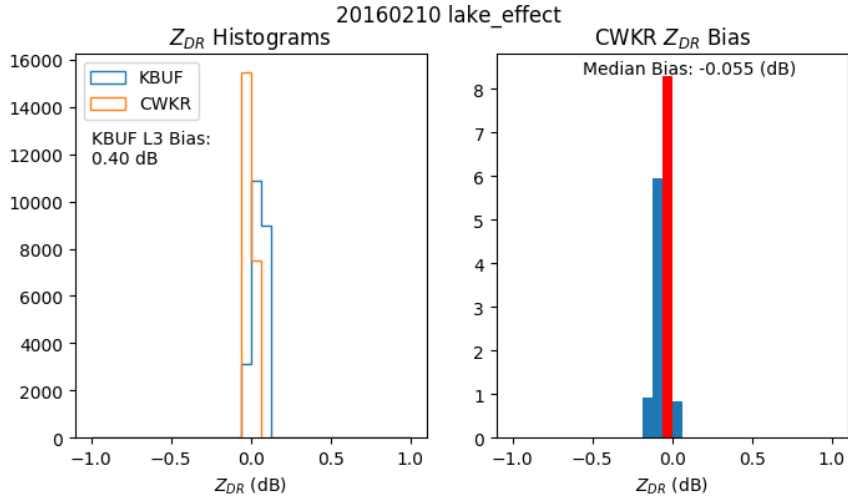


Figure 3.36: Histograms of Z_{DR} (left), Z_{DR} bias at CWKR, determined by subtracting the gridded, bias adjusted Z_{DR} at KBUF from the Z_{DR} at CWKR. Both datasets exclude matched points with $KDE < 2$.

3.1.10 15 December 2016 - Synoptic

A deep longwave trough is centered over Southern Ontario, with an Arctic airmass in place over the Great Lakes region. With meager moisture in place, a post-frontal trough manages to squeeze out some passing snow-showers. As indicated by Figure 3.37, the spatial patterns of Z_{eH} are in very good agreement. In contrast, Figure 3.38 shows two very noisy Z_{DR} fields. Even with the small sample size, Figure 3.39 shows that decent fits are achieved for both moments. Meanwhile, the histogram in Figure 3.40 shows that the estimate of bias at CWKR is large, with a median value of -0.465 dB. This case is an outlier; the source of this large bias will be discussed in the next chapter.

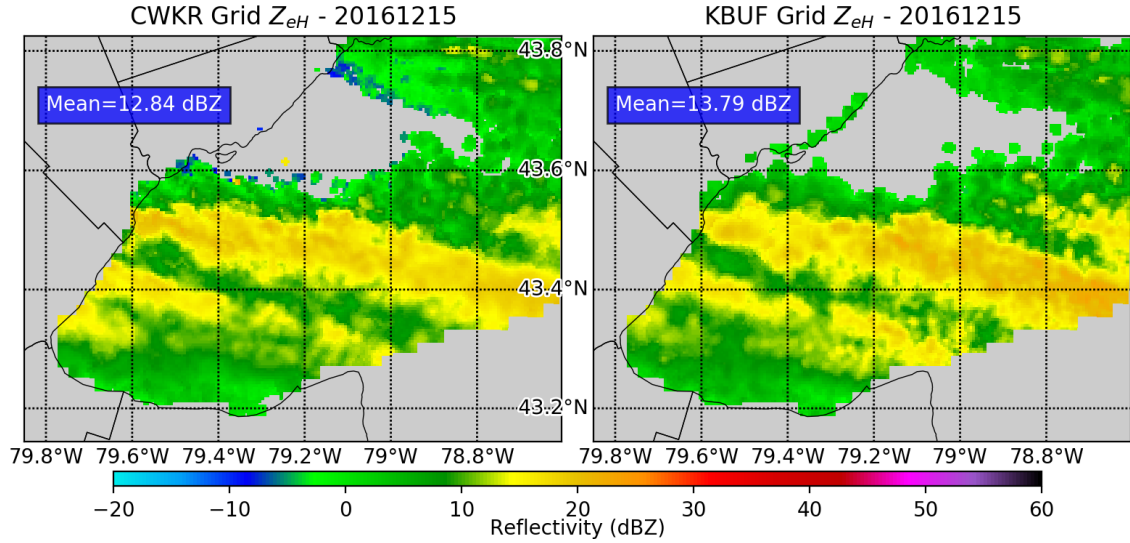


Figure 3.37: Gridded Z_{eH} comparison for 15 December 2016. Time-average of all admitted scans.

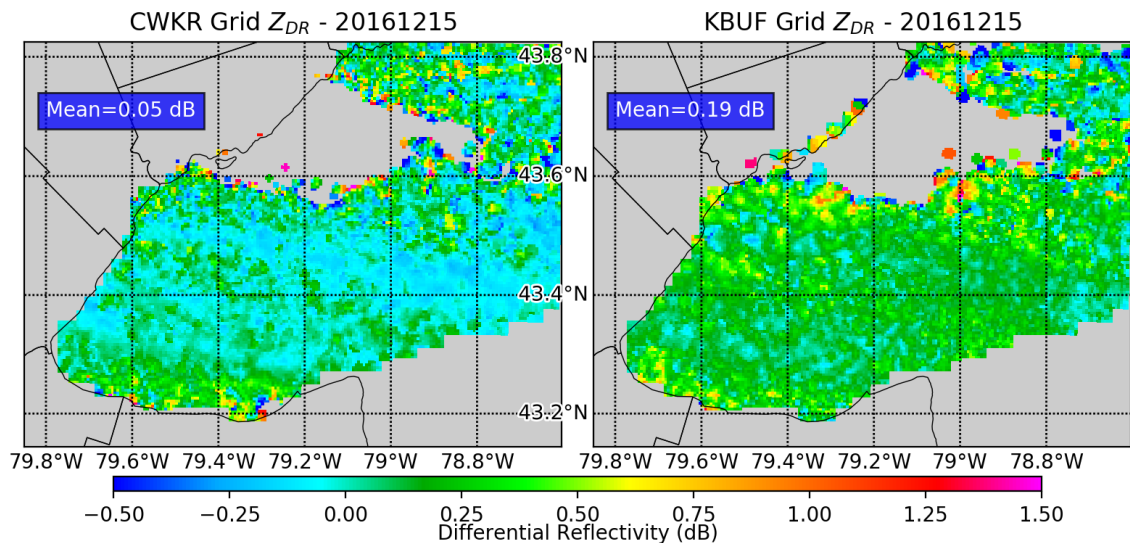


Figure 3.38: Gridded Z_{DR} comparison for 15 December 2016. Time-average of all admitted scans.

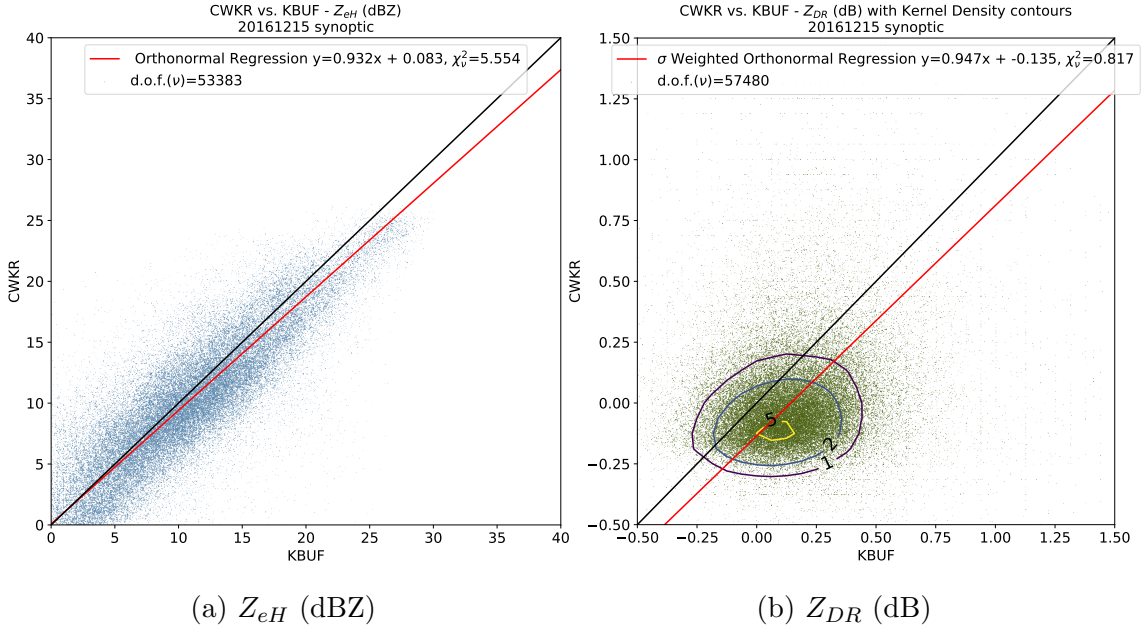


Figure 3.39: Direct comparisons for 15 December 2016. Dataset includes all admitted grid cells.

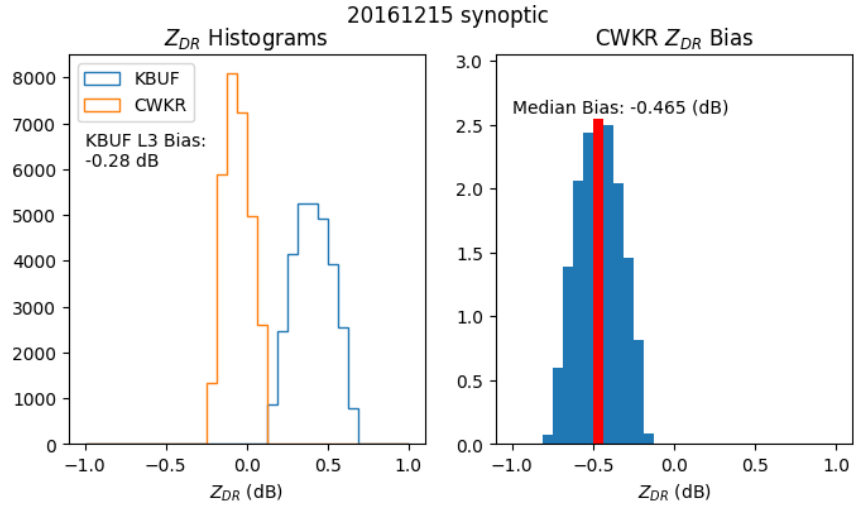


Figure 3.40: Histograms of Z_{DR} (left), Z_{DR} bias at CWKR, determined by subtracting the gridded, bias adjusted Z_{DR} at KBUF from the Z_{DR} at CWKR. Both datasets exclude matched points with KDE < 2.

3.2 Z_{eH} Subset Comparisons

Now that all the cases have been presented individually, two subsets are created for comparison. The first consists of the five lake-effect events, the subset of interest, as compared with the five synoptic events, which act as a control subset. A comparison of these subset is shown in Figure 3.41, with a scatter-plot of KBUF Z_{eH} data versus CWKR on the common grid. Figure 3.41a is the subset of synoptic events while Figure 3.41b is the subset of lake-effect events. These results show that lake-effect snow events achieve a better match between the radars than synoptic events; there is a sample size caveat due to synoptic subset only containing about a third of the matched points than those in the synoptic subset. Another result shown in Figure 3.41 is that CWKR is slightly under-reporting reflectivity in the 15-25 dBZ range for lake-effect events, while it over-reports for synoptic events. In order to examine this further, we turn to Figure ??, revealing heavier banding closer to KBUF (south of 43.4° N and east of 79° W) in lake-effect events. Due to the bands location farther away from CWKR, its beam is most likely overshooting this shallow lake effect band. This is confirmed by the pattern in the reflectivity differences, which reveals a stronger range dependency in lake-effect events than synoptic. Another notable feature in Figure ?? is the resolution of finer scale features by CWKR is superior, especially for the lake-effect banding patterns around mid-lake. This is likely a function of its narrower physical beamwidth.

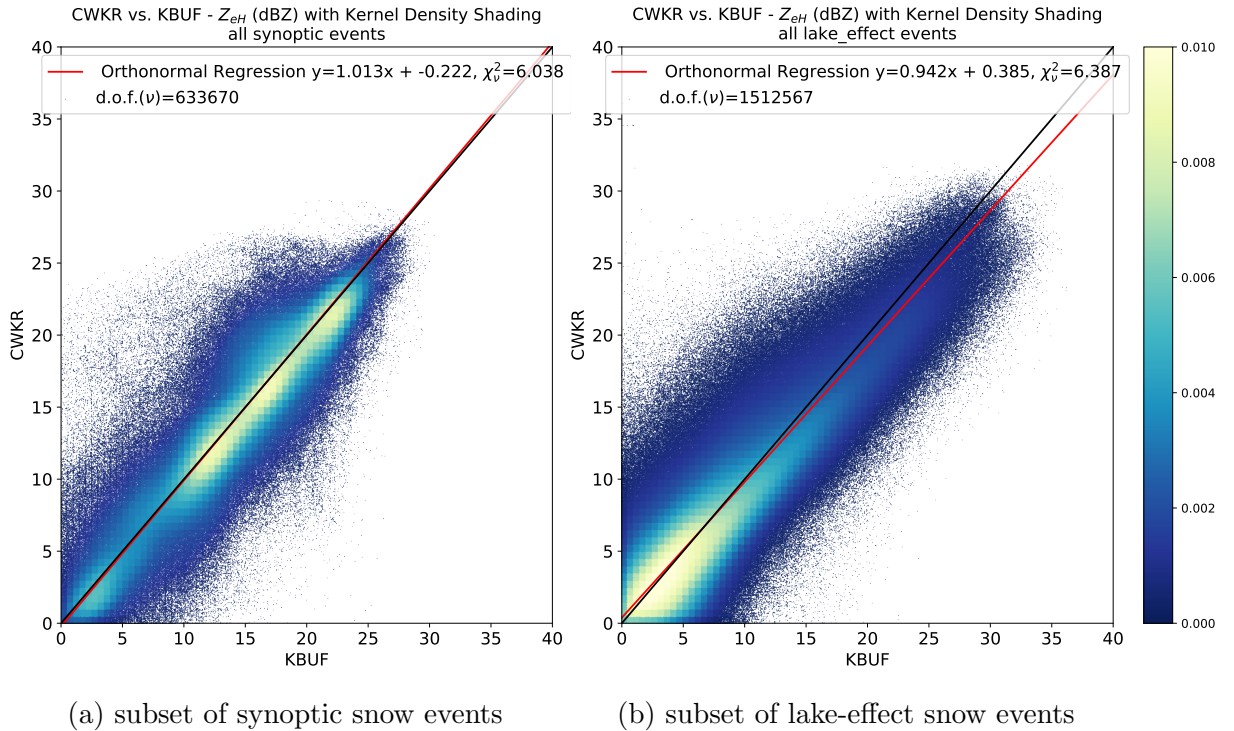


Figure 3.41: Scatter-plots of CWKR versus KBUF grid analyzed reflectivity, with Kernel Density Estimation shading. The red line is an Orthonormal Linear Regression, with a black identity line.

A Appendix A

A.1 Upper-Air Charts

Images provided by the NOAA/ESRL Physical Science Division, Boulder, Colorado.

Original data can be found at <http://www.esrl.noaa.gov/psd/>.

A.2 Skew-T Charts

Raw sounding data provided by the Department of Atmospheric Science at the University of Wyoming. Original data can be found at <http://weather.uwyo.edu/upperair/sounding.html>.

A.3 Sounding Climatology

Images provided by the National Weather Service Storm Prediction Center in Norman, Oklahoma. Original data can be found at <http://www.spc.noaa.gov/exper/soundingclimo/>.

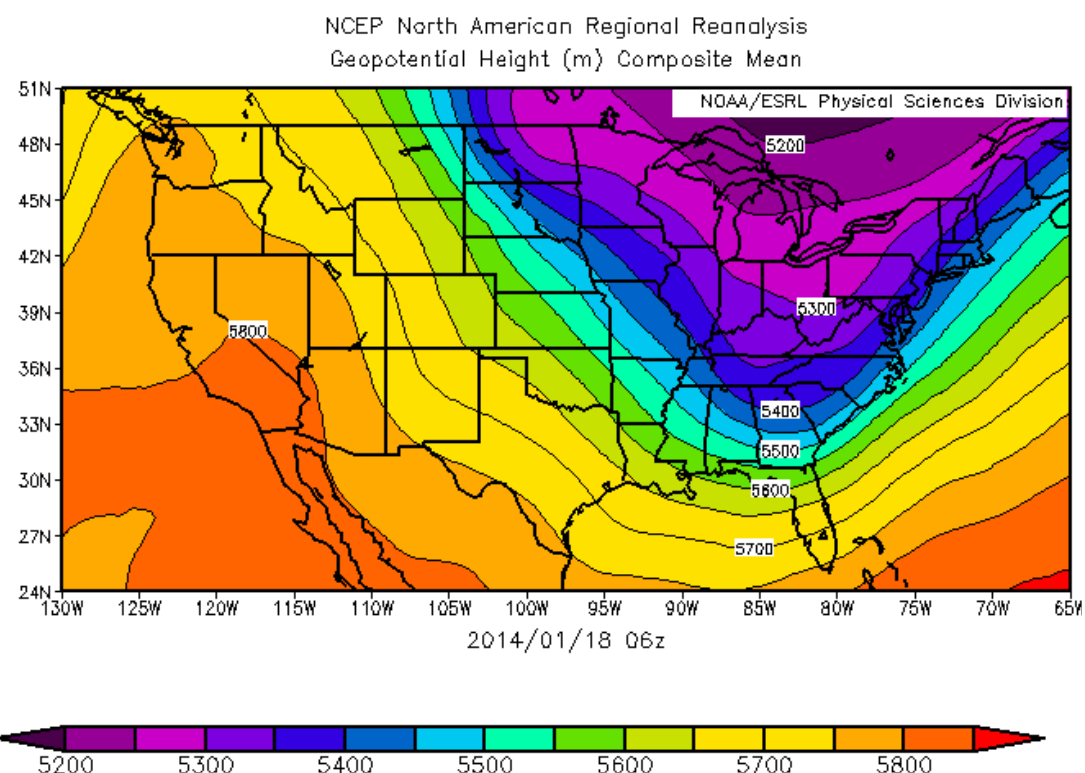


Figure A.1: 500mb Geopotential Height at 06Z 18 January 2014.

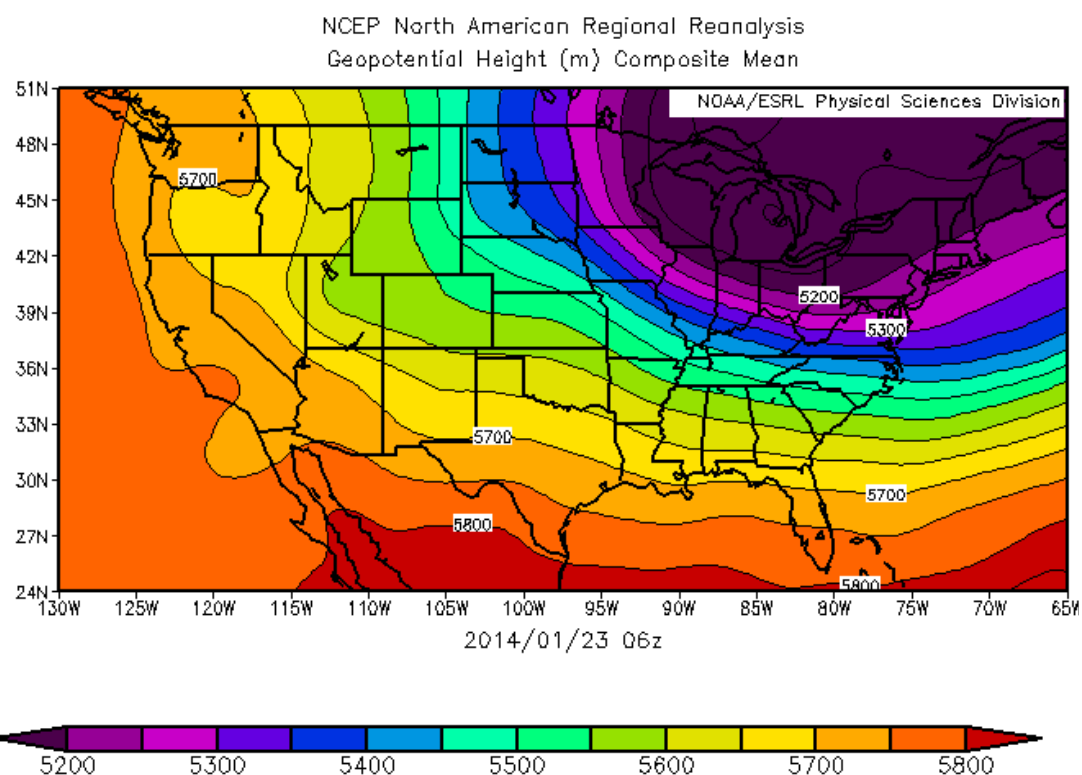


Figure A.2: 500mb Geopotential Height at 06Z 23 January 2014

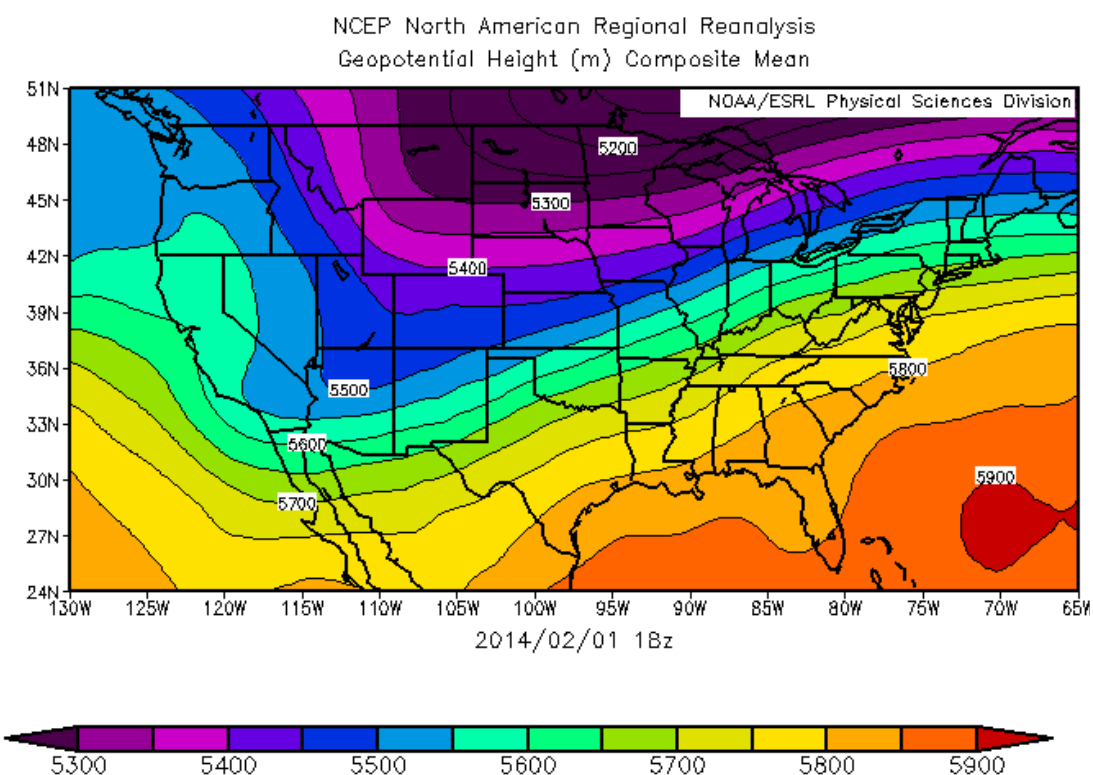


Figure A.3: 500mb Geopotential Height at 18Z 1 February 2014.

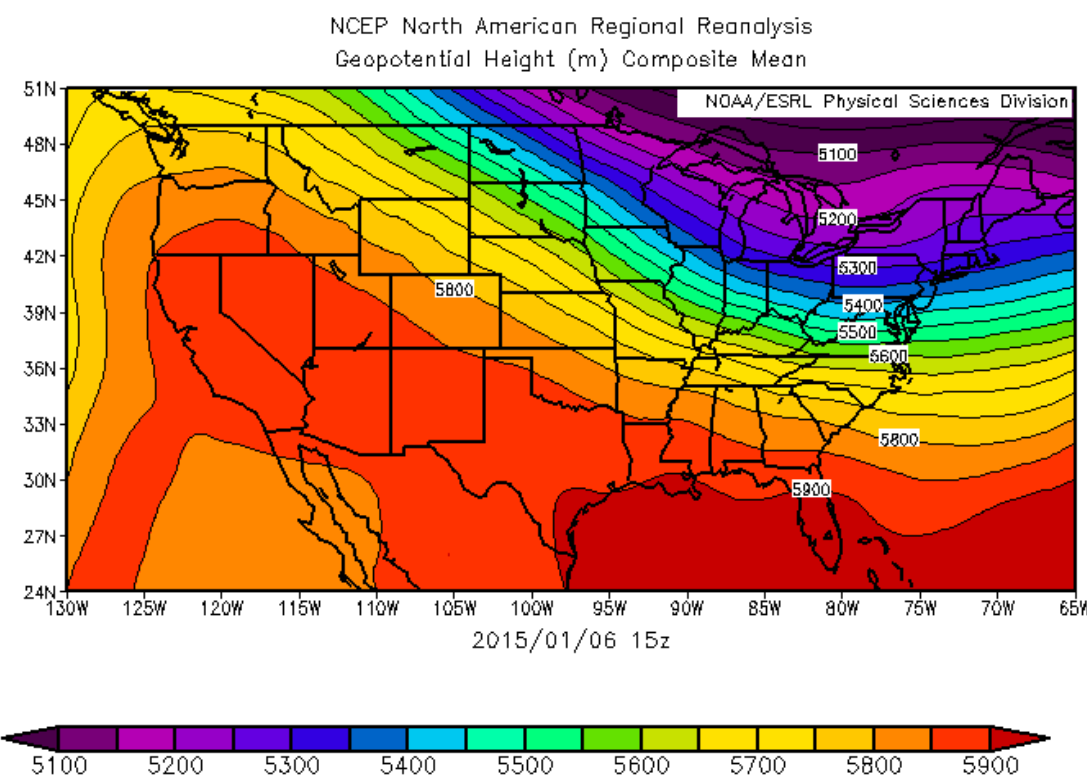


Figure A.4: 500mb Geopotential Height at 15Z 6 January 2015.

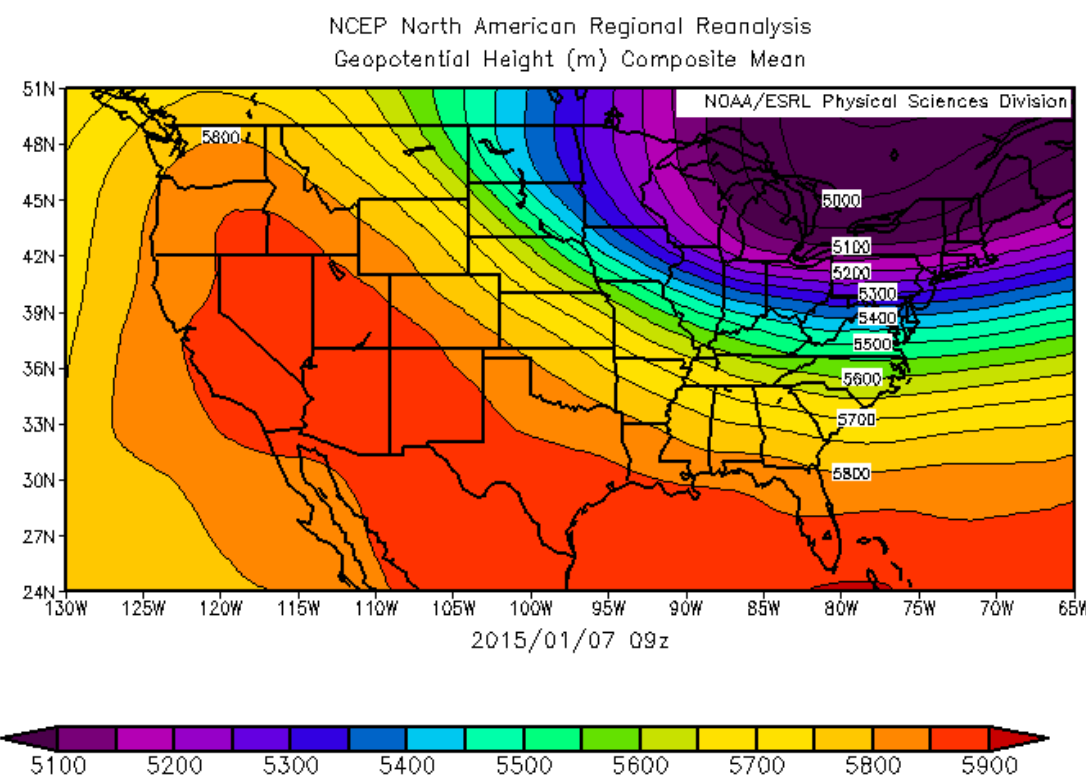


Figure A.5: 500mb Geopotential Height at 09Z 7 January 2015.

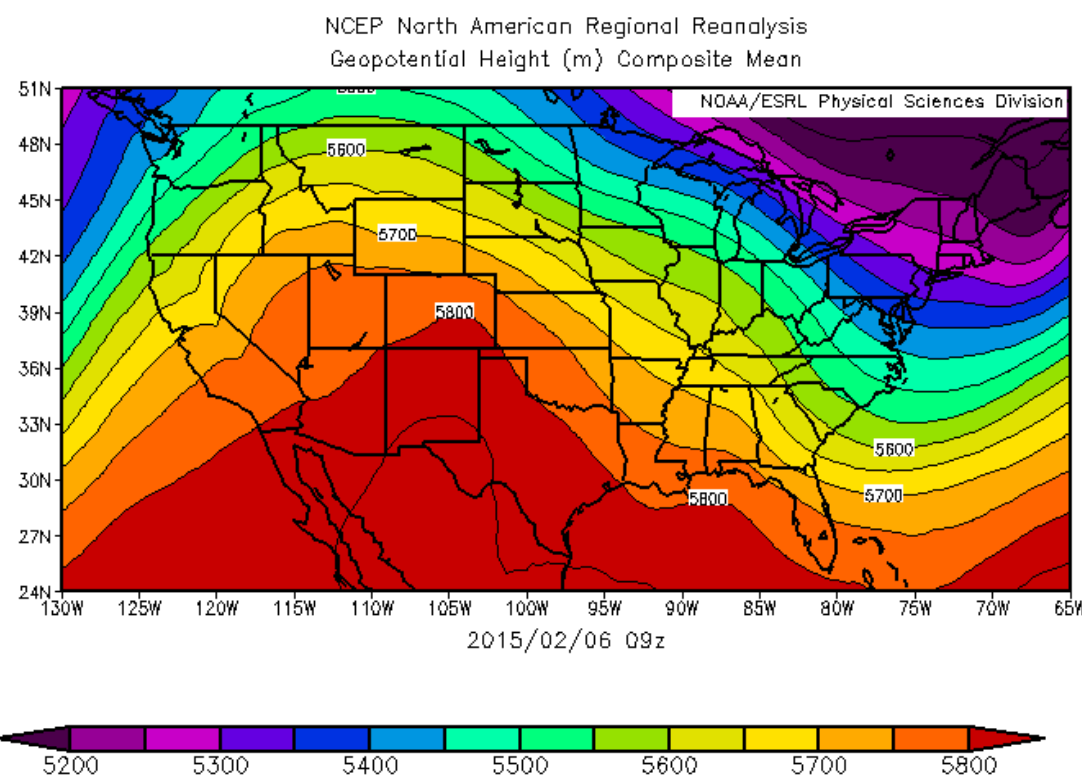


Figure A.6: 500mb Geopotential Height at 09Z 6 February 2015.

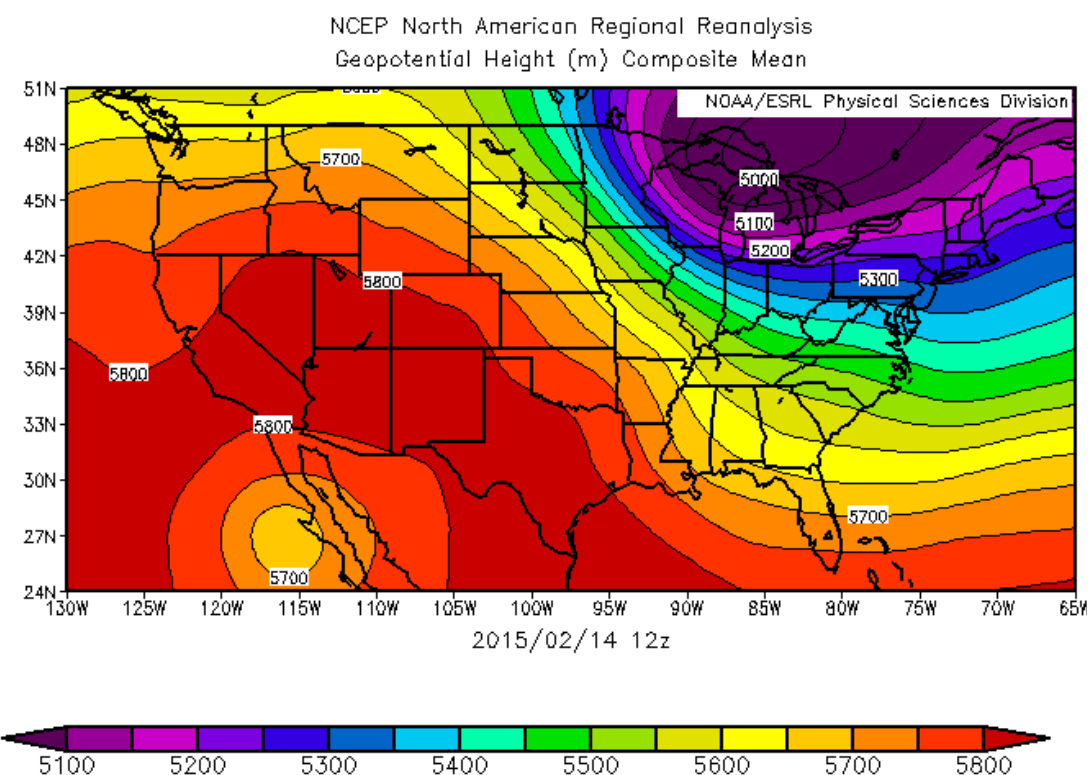


Figure A.7: 500mb Geopotential Height at 12Z 14 February 2015.

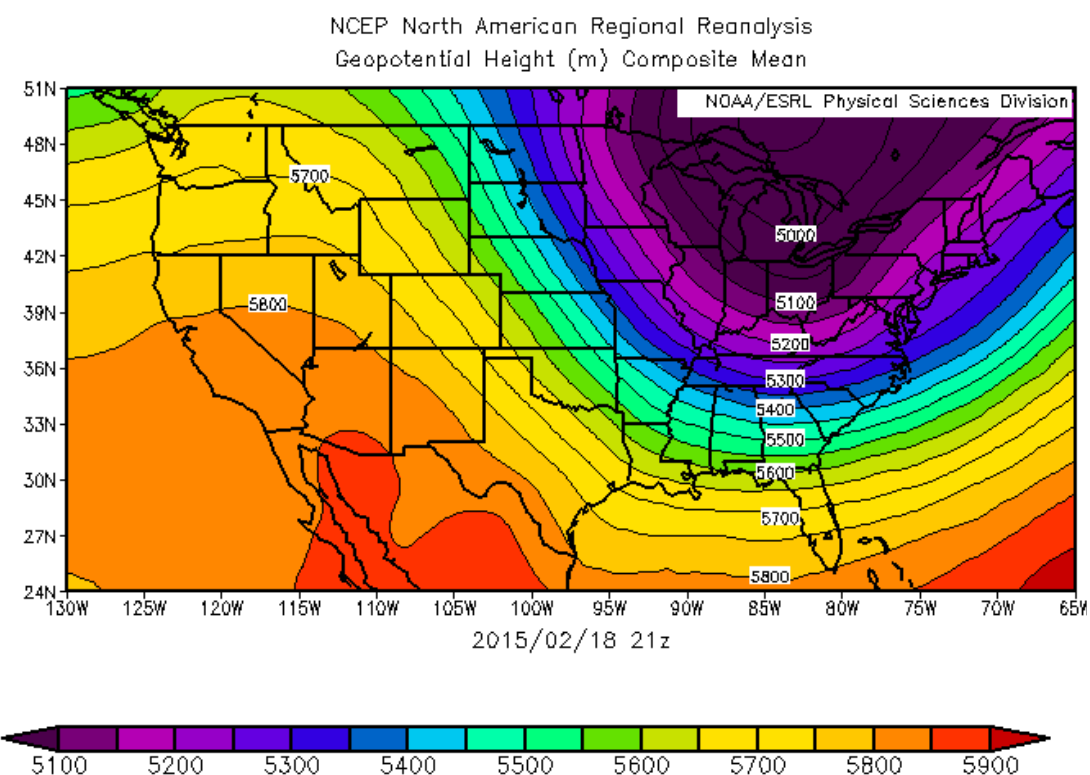


Figure A.8: 500mb Geopotential Height at 21Z 18 February 2015.

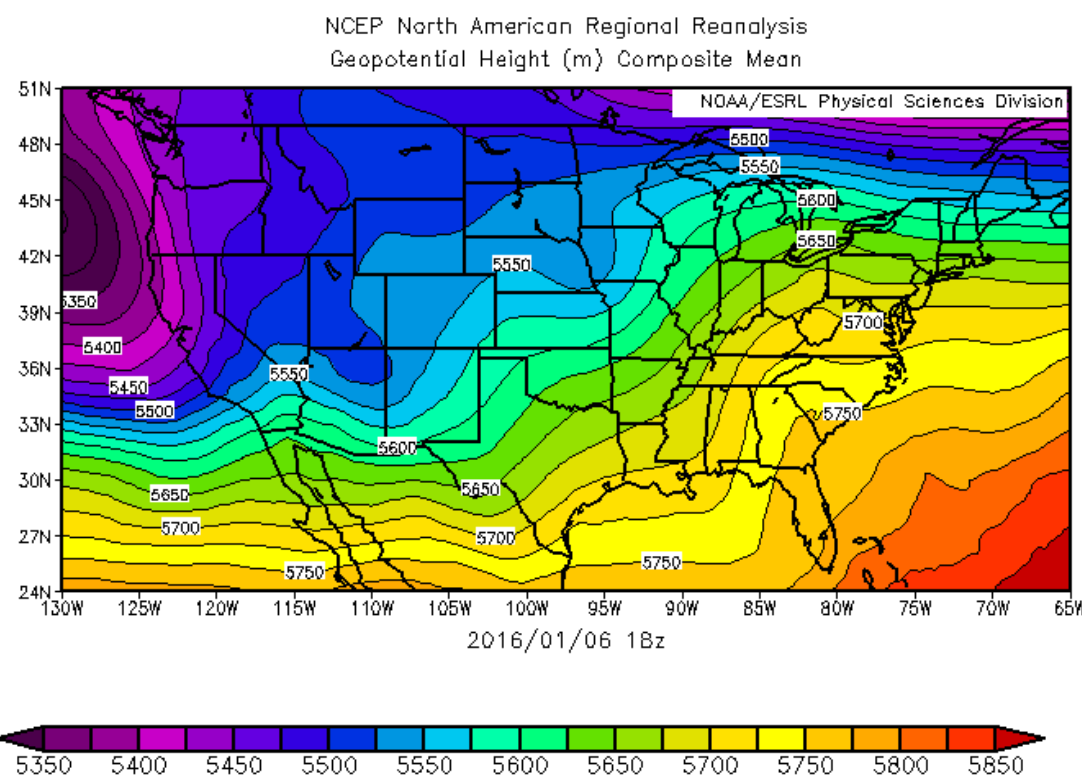


Figure A.9: 500mb Geopotential Height at 18Z 10 February 2016.

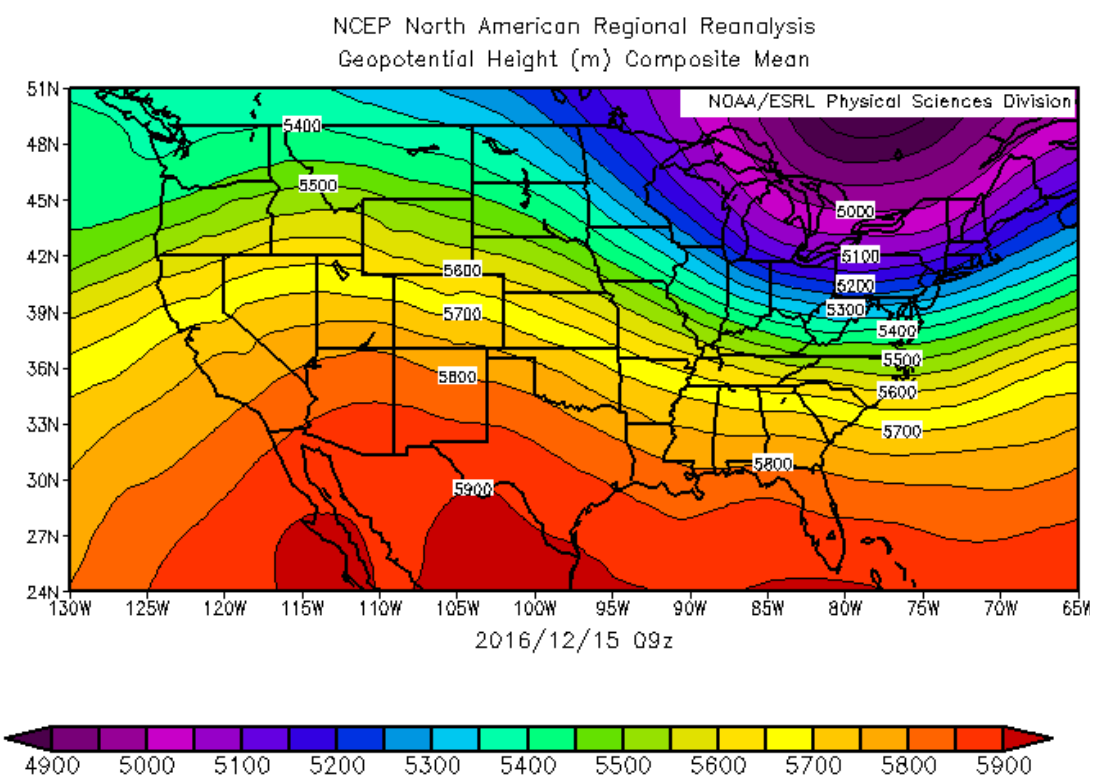


Figure A.10: 500mb Geopotential Height at 09Z 15 December 2016.

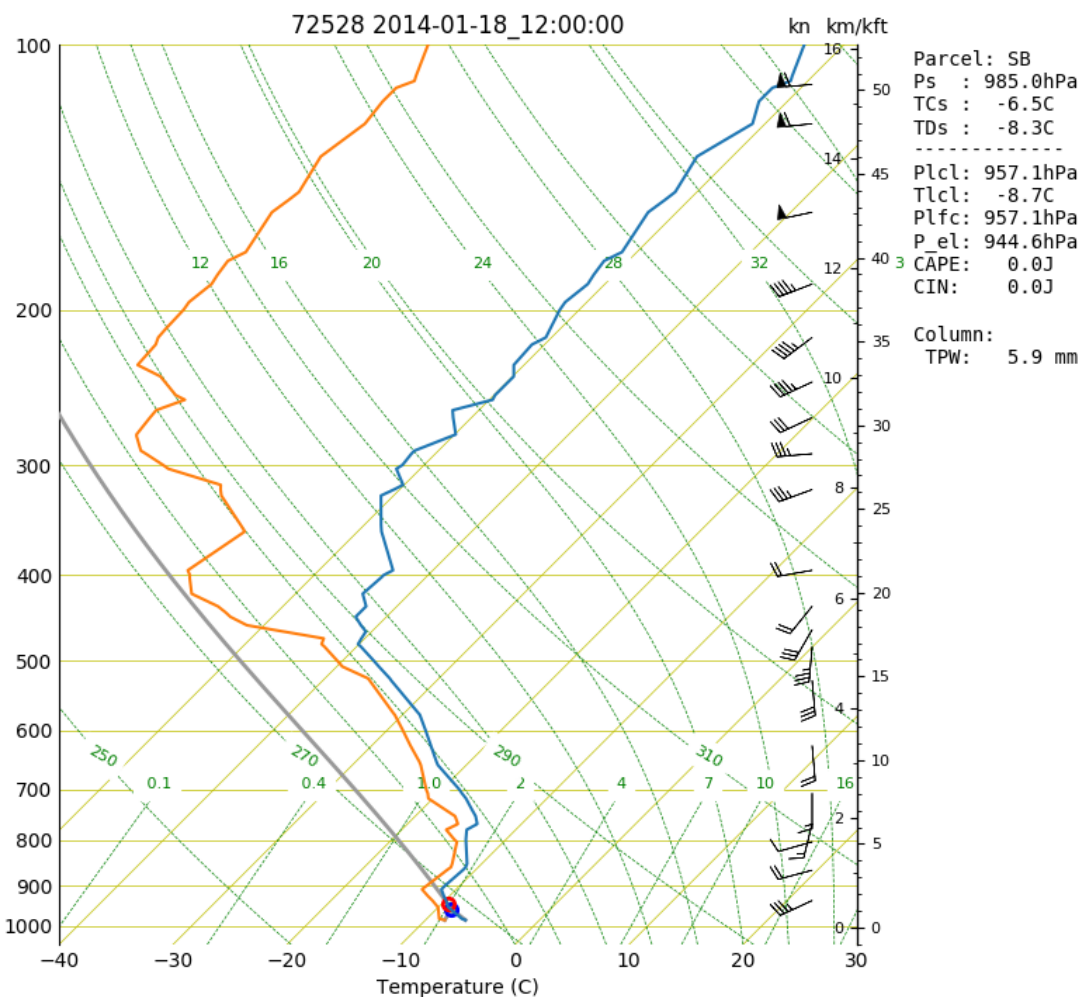


Figure A.11: SkewT/Log-P Chart from the BUF Radiosonde launched at 12Z 18 January 2014

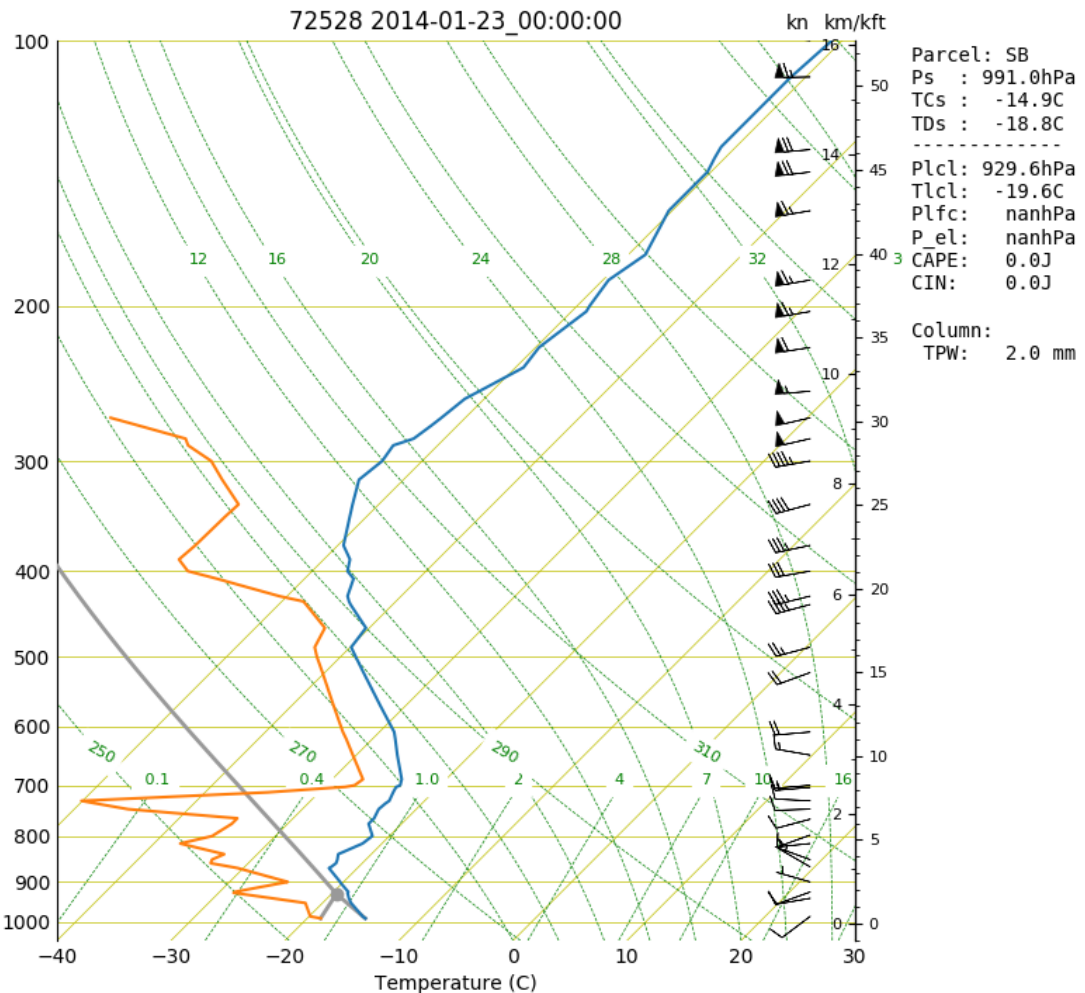


Figure A.12: SkewT/Log-P Chart from the BUF Radiosonde launched at 00Z 23 January 2014

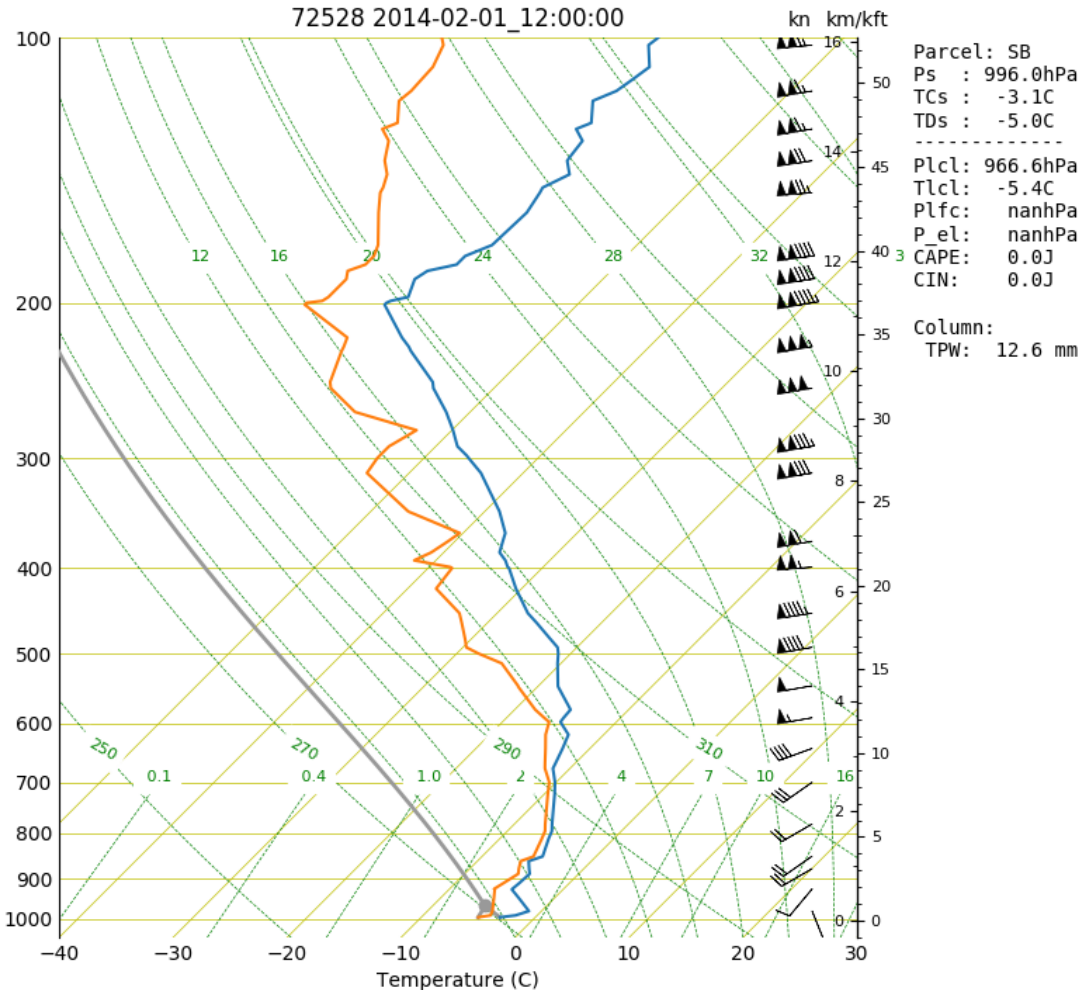


Figure A.13: SkewT/Log-P Chart from the BUF Radiosonde launched at 12Z 1

February 2014

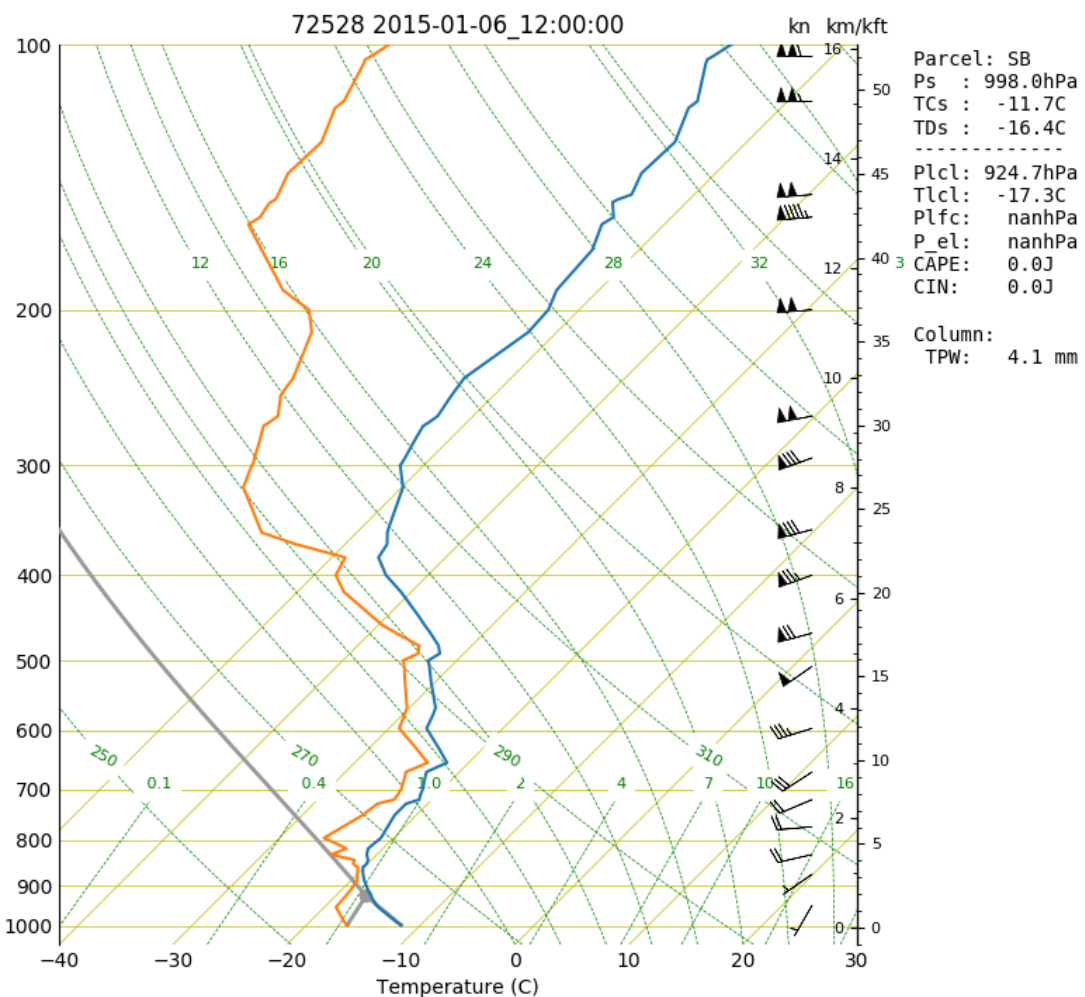


Figure A.14: SkewT/Log-P Chart from the BUF Radiosonde launched at 00Z 6 January 2015

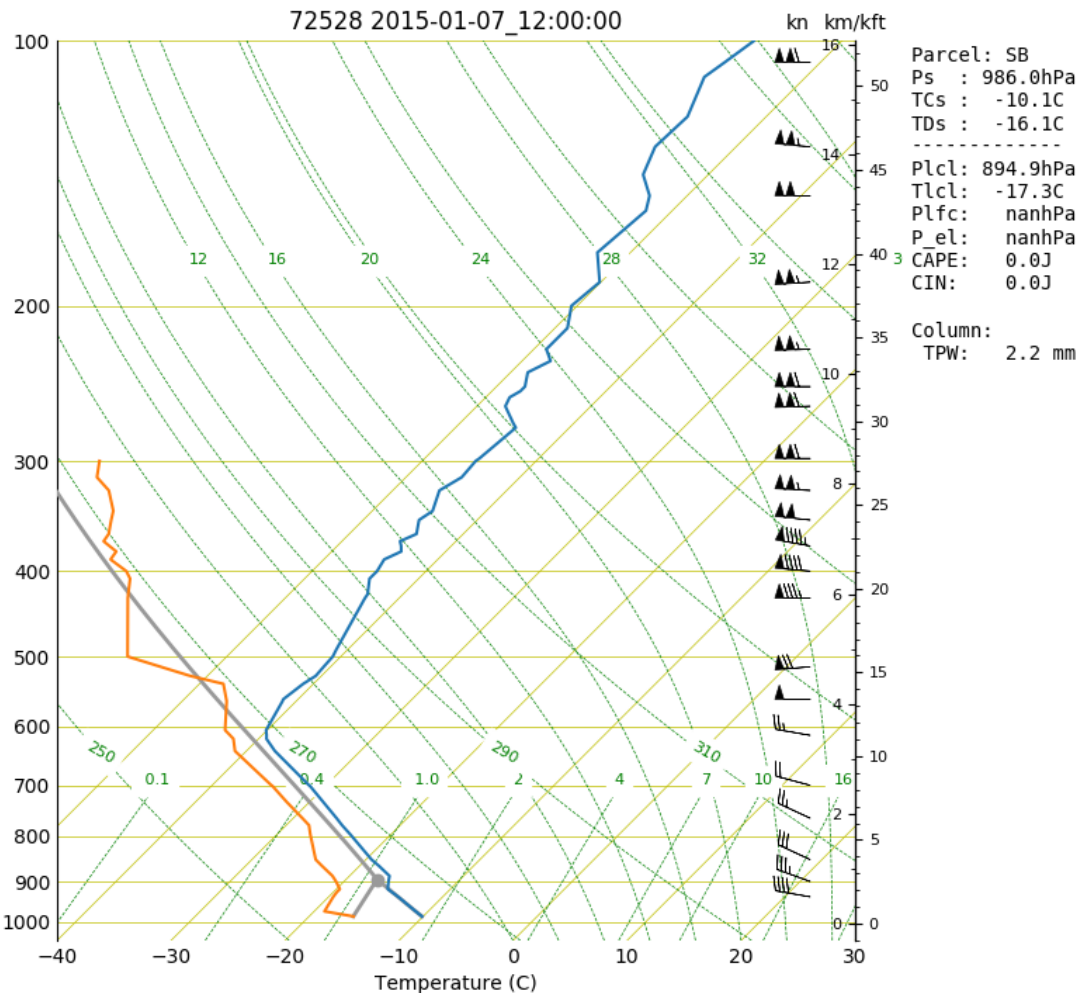


Figure A.15: SkewT/Log-P Chart from the BUF Radiosonde launched at 12Z 7 January 2015

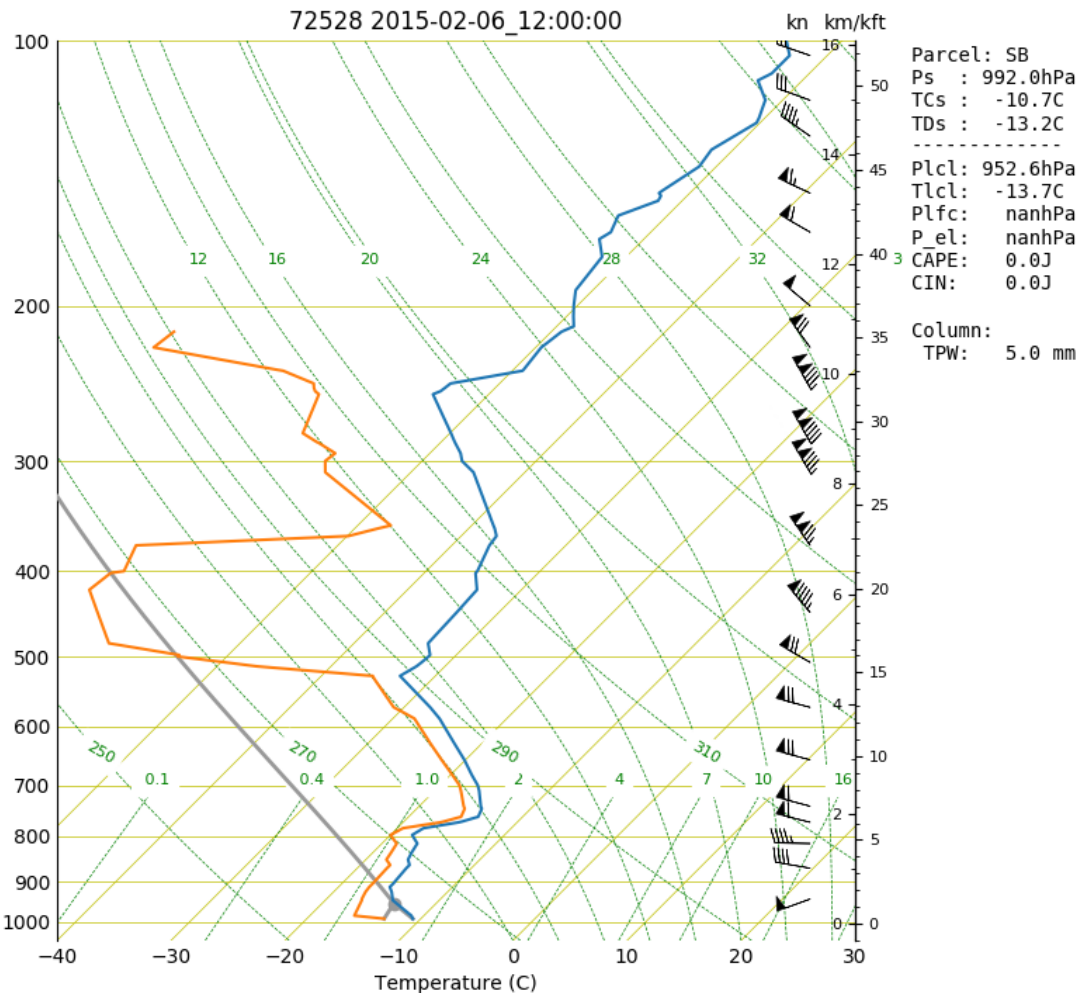


Figure A.16: SkewT/Log-P Chart from the BUF Radiosonde launched at 00Z 6

February 2015

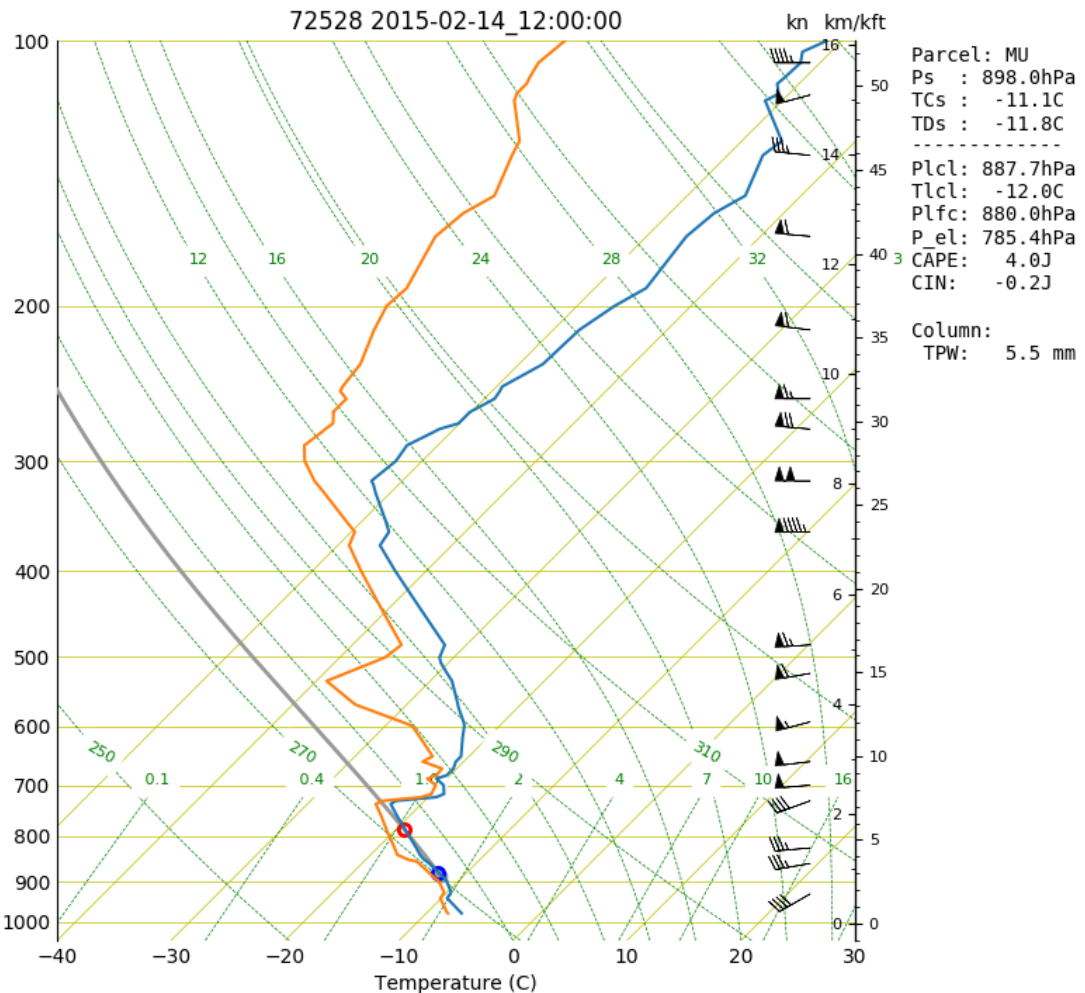


Figure A.17: SkewT/Log-P Chart from the BUF Radiosonde launched at 12Z 14

February 2015

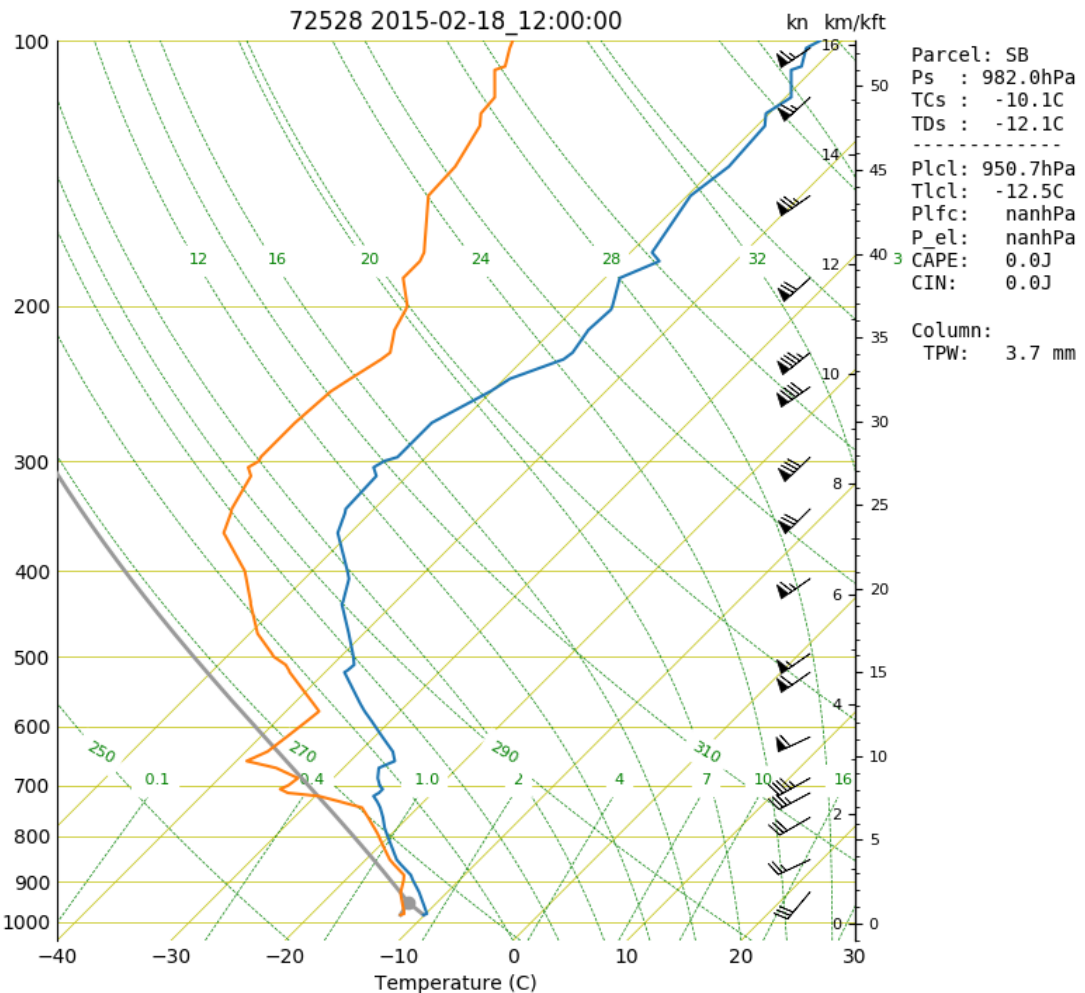


Figure A.18: SkewT/Log-P Chart from the BUF Radiosonde launched at 00Z 18 February 2015

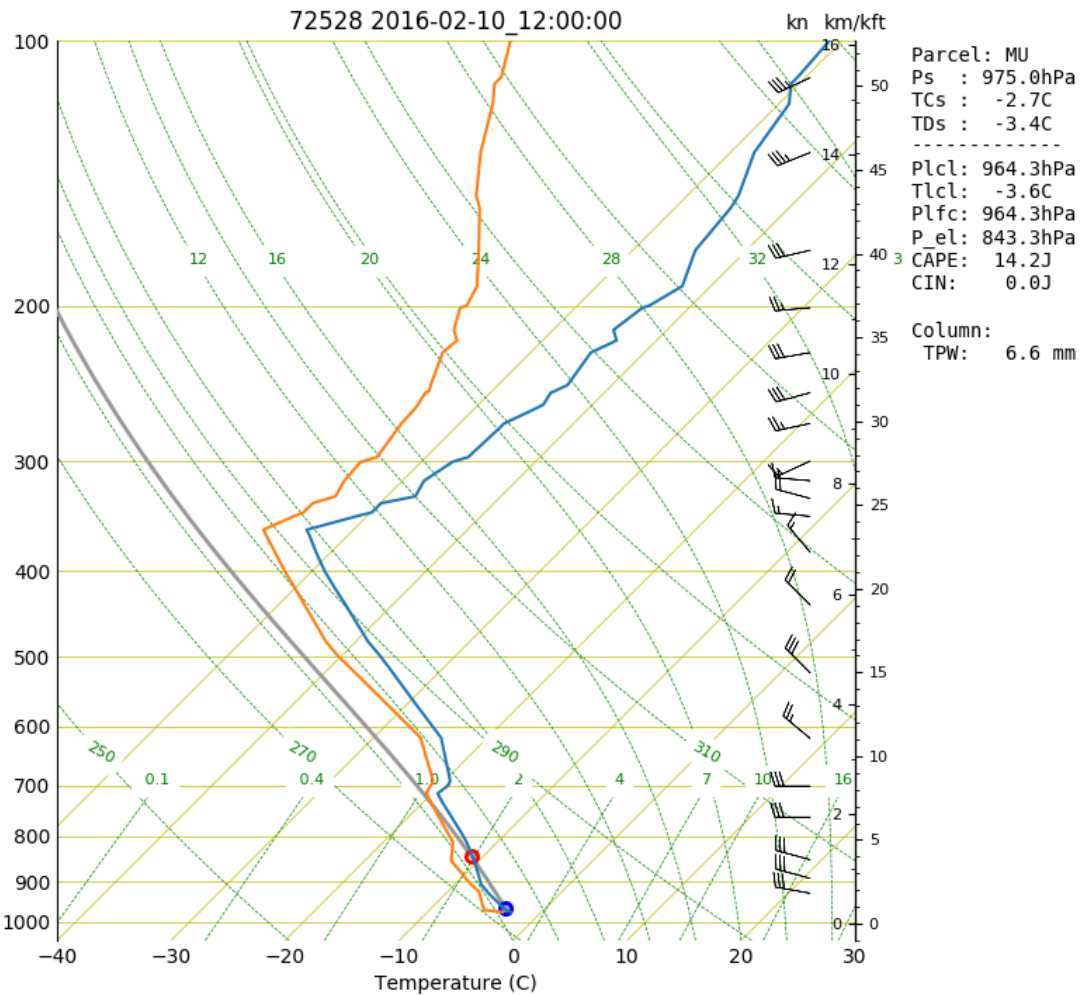


Figure A.19: SkewT/Log-P Chart from the BUF Radiosonde launched at 12Z 10

February 2016

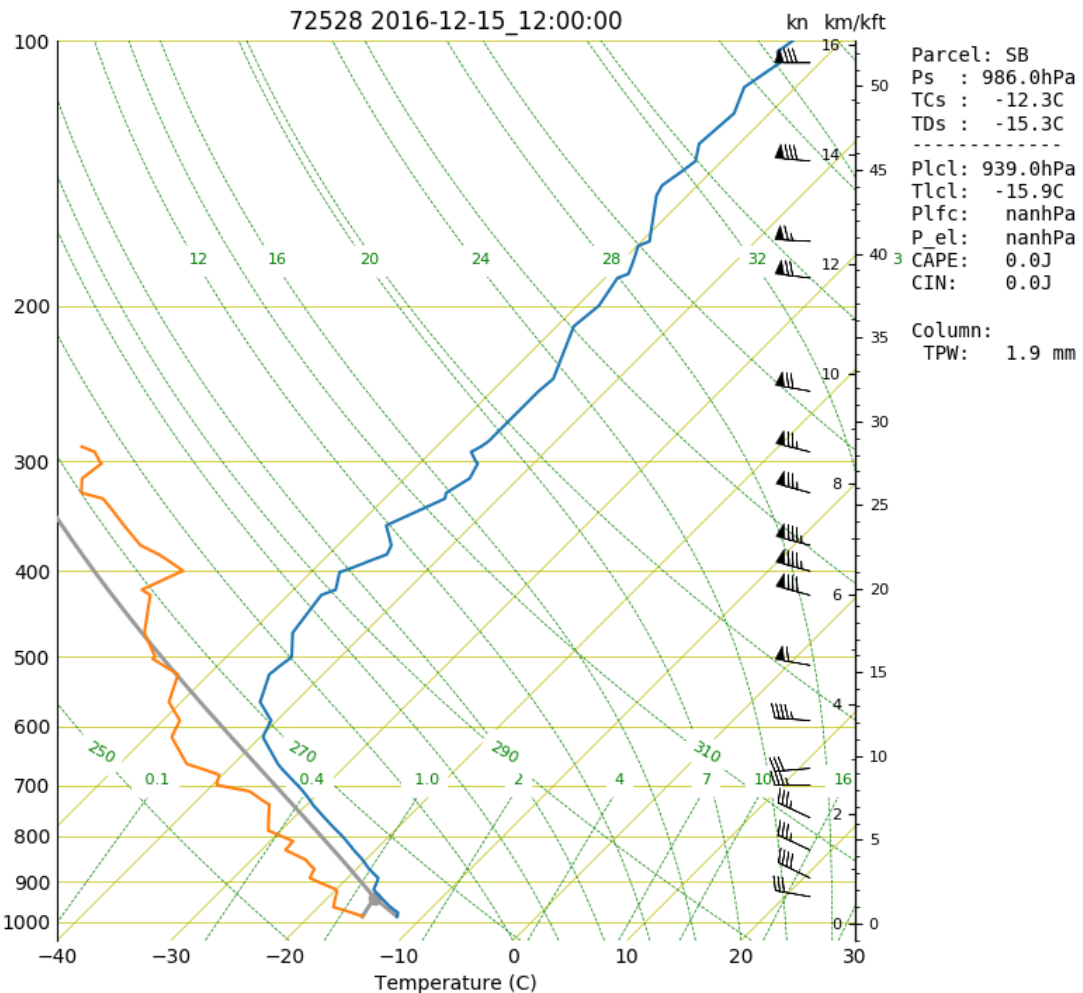


Figure A.20: SkewT/Log-P Chart from the BUF Radiosonde launched at 12Z 15

December 2016

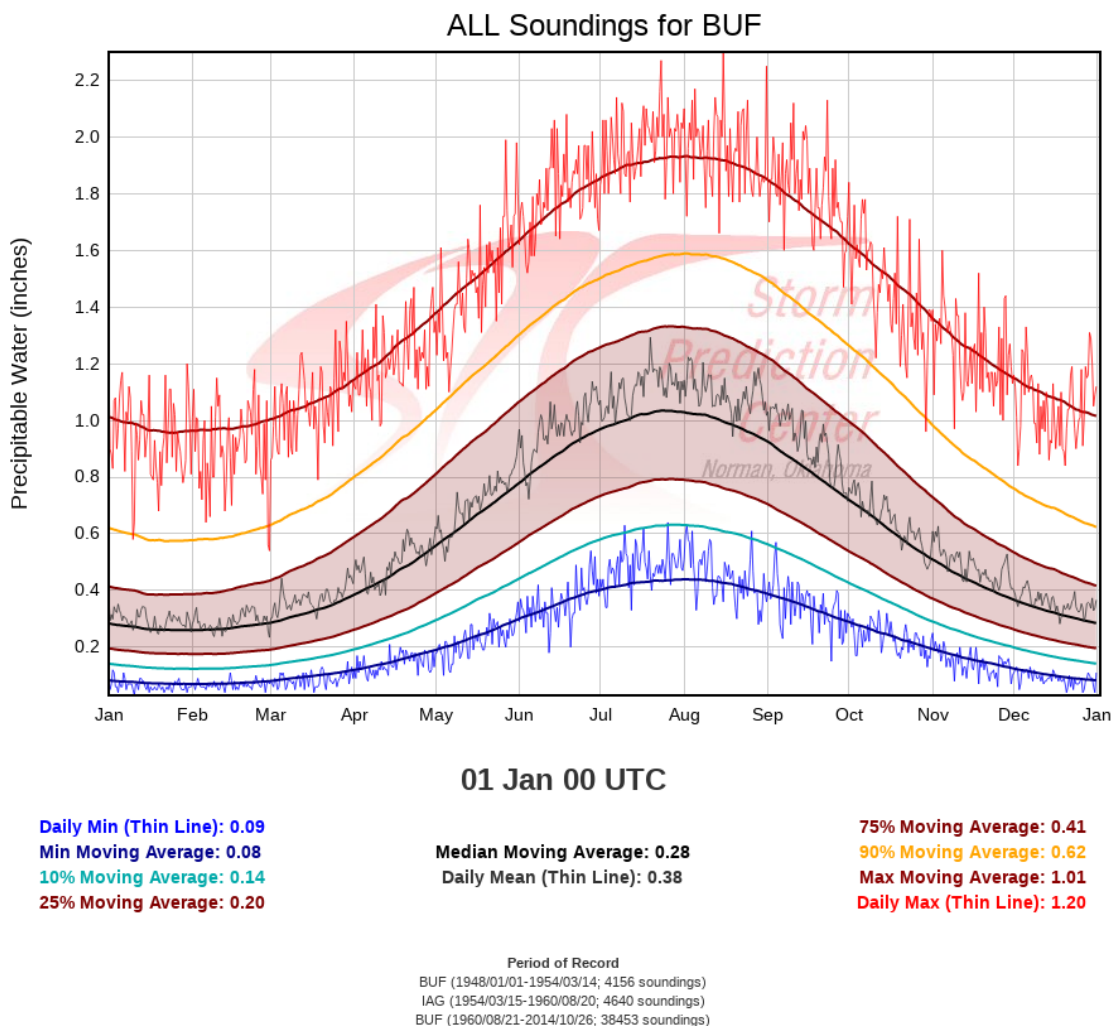


Figure A.21: Sounding Precipitable Water Climatology for BUF

Bibliography

- Fabry, F., 2015: *Radar Meteorology: Principles and Practice*. Cambridge University Press, 256 pp.
- Hassan, D., P. A. Taylor, and G. A. Isaac, 2017: Snowfall Rate Estimation using C-Band Polarimetric Radars. *Meteor. Appl.*, **24** (1), 142–156, URL <http://doi.org/10.1002/met.1613>.
- Helmus, J. J. and S. M. Collis, 2016: The Python ARM Radar Toolkit (Py-ART), a Library for Working with Weather Radar Data in the Python Programming Language. *JORS*, **4** (1), e25, URL <http://doi.org/10.5334/jors.119>.
- Hubbert, J. and F. Pratte, 2006: Differential Reflectivity Calibration for Nexrad. *2006 IEEE International Symposium on Geoscience and Remote Sensing*, 519–522, URL <https://doi.org/10.1109/IGARSS.2006.138>.
- Markovsky, I. and S. V. Huffel, 2007: Overview of total least-squares methods. *Elsevier BV*, URL <http://doi.org/10.1016/j.sigpro.2007.04.004>.
- Pauley, P. M. and X. Wu, 1990: The theoretical, discrete, and actual response of the Barnes objective analysis scheme for one- and two-dimensional fields. *Mon. Wea. Rev.*, **118** (5), 1145–1164, URL [http://doi.org/10.1175/1520-0493\(1990\)118<1145:TTDAAR>2.0.CO;2](http://doi.org/10.1175/1520-0493(1990)118<1145:TTDAAR>2.0.CO;2).
- Rogers, R. and M. Yau, 1989: *A Short Course in Cloud Physics*, Vol. 113. Elsevier, 290 pp.
- Silverman, B. W., 1986: *Density Estimation for Statistics and Data Analysis*, Vol. 26. Chapman and Hall, 176 pp.
- Torres, S. and C. Curtis, 2007: Initial Implementation of Super-Resolution Data on the NEXRAD Network. *23rd Conf. on IIPS*, San Antonio, TX, Amer. Meteor. Soc., 5B.10, URL https://ams.confex.com/ams/87ANNUAL/techprogram/paper_116240.htm.

Zittel, W. D., R. R. Lee, L. M. R. J. G. Cunningham, J. Schultz, and R. L. Ice, 2015: Geographical and Seasonal Availability of Light Rain, Dry Snow, and Bragg Scatter to Estimate WSR-88D z_{DR} System Bias. *31st Conf. on EIP*, Phoenix, AZ, Amer. Meteor. Soc., 11.2, URL <https://ams.confex.com/ams/95Annual/webprogram/Paper265374.html>.

Zrnic, D., V. M. Melnikov, and J. K. Carter, 2006: Calibrating Differential Reflectivity on the WSR-88D. *Journal of Atmospheric and Oceanic Technology*, **23** (7), 944–951, doi:10.1175/JTECH1893.1, URL <https://doi.org/10.1175/JTECH1893.1>.